Geological setting of Earth's oldest fossils in the ca. 3.5Ga Dresser Formation, Pilbara Craton, Western Australia

Martin J. van Kranendonk, Pascal Philippot, Kevin Lepot, Simon Bodorkos, Franco Pirajno

Geological setting of Earth's oldest fossils in the ca. 3.5 Ga Dresser Formation, Pilbara Craton, Western Australia

Martin J. Van Kranendonk [a,*], Pascal Philippot [b], Kevin Lepot [b], Simon Bodorkos [a,1], Franco Pirajno [a]

[a] *Geological Survey of Western Australia, 100 Plain Street, East Perth, Western Australia 6004, Australia*
[b] *Laboratoire Géobiosphère Actuelle et Primitive, Institut de Physique du Globe de Paris, Case 89, 4 place Jussieu, 75252 Paris Cedex 05, France*

Detailed stratigraphic, petrographic, and zircon U–Pb geochronological data are provided for surface outcrops and newly obtained, unweathered drillcore intersections of Earth's oldest fossiliferous sedimentary rocks, the lowermost chert–barite unit of the ca. 3.5 Ga Dresser Formation, Warrawoona Group, Pilbara Craton.

Results show that the ~8 m thick unit at the drilling locality consists of thinly bedded, originally micritic carbonates deposited under quiet water conditions that are interbedded with volcaniclastic conglomerates and coarse polymict conglomerates (diamictites) deposited during periods of tectonic instability. The presence of rapid vertical and lateral facies changes, tilted bedding in some members, and internal erosional unconformities, combined with analysis of fault offsets, indicate that tectonically unstable periods were caused by growth faulting. Intense hydrothermal fluid flow accompanied episodes of growth faulting and resulted in pulsed, repeated precipitation of silica ± barite ± sphalerite that alternated with precipitation of pyrite. Clasts of hydrothermal minerals in sandstone and coarse, polymict conglomerate beds at several levels within the unit highlight the repeated nature of hydrothermal fluid circulation during sediment accumulation. Hydrothermal fluid circulation caused widespread acid–sulfate alteration of the footwall, extensive replacement of the newly deposited carbonate sediments by hydrothermal precipitates, and crystallization of hydrothermal chert–barite–pyrite in veins perpendicular to bedding in the footwall and parallel to bedding in the sedimentary unit. The combined evidence points to deposition of the chert–barite unit within an active volcanic caldera. A 10 cm thick bed of felsic volcaniclastic tuff within finely bedded carbonates near the top of the unit has yielded a maximum age of deposition of 3481.0 ± 3.6 Ma (2σ uncertainty), confirming earlier Pb–Pb age data for the antiquity of these rocks.

Putative signs of life are present as stratiform, columnar, domical, and coniform stromatolitic laminates at various levels throughout the unit. Petrographic observations show that red- and black-weathering stromatolitic laminates on the surface consist of pyrite in unweathered drillcore material. Observation of local relics of carbonate between pyrite crystals in these laminates indicates a carbonate protolith prior to replacement by hydrothermal pyrite, which provides support for a biological origin of stromatolitic laminates. Further support is provided by clasts of laminated carbonaceous material in thinly bedded, primary micritic carbonates.

Textural analysis of jaspilitic "cherts" near the top of the unit reveal haematite as tiny crystals within recrystallized siderite/dolomite rhombs in carbonate beds affected by hydrothermal silica alteration. The presence of unaltered diagenetic pyrite crystals in the haematite-altered siderite indicates that alteration did *not* result from oxidizing fluids. Rather, haematite alteration is interpreted as the result of an increase in pH during diagenetic alteration by mildly reducing, silica-rich fluids associated with eruption of overlying basalts, possibly with the influence of microbial activity. This has important implications for the origin of jaspilitic cherts throughout the early Archean record and for atmospheric conditions of early Earth.

1. Introduction

Controversy exists regarding the geological setting and biogenicity of Earth's oldest stromatolites (Walter et al., 1980) and microfossils (Ueno et al., 2001a,b, 2004) in bedded chert–barite deposits of the ca. 3.5 Ga Dresser Formation in the North Pole Dome

* Corresponding author. Tel.: +61 8 9222 3631; fax: +61 8 9222 3633.
E-mail address: martin.vankranendonk@doir.wa.gov.au (M.J. Van Kranendonk).
[1] Now at: Geoscience Australia, GPO Box 378, Canberra, ACT 2601, Australia.

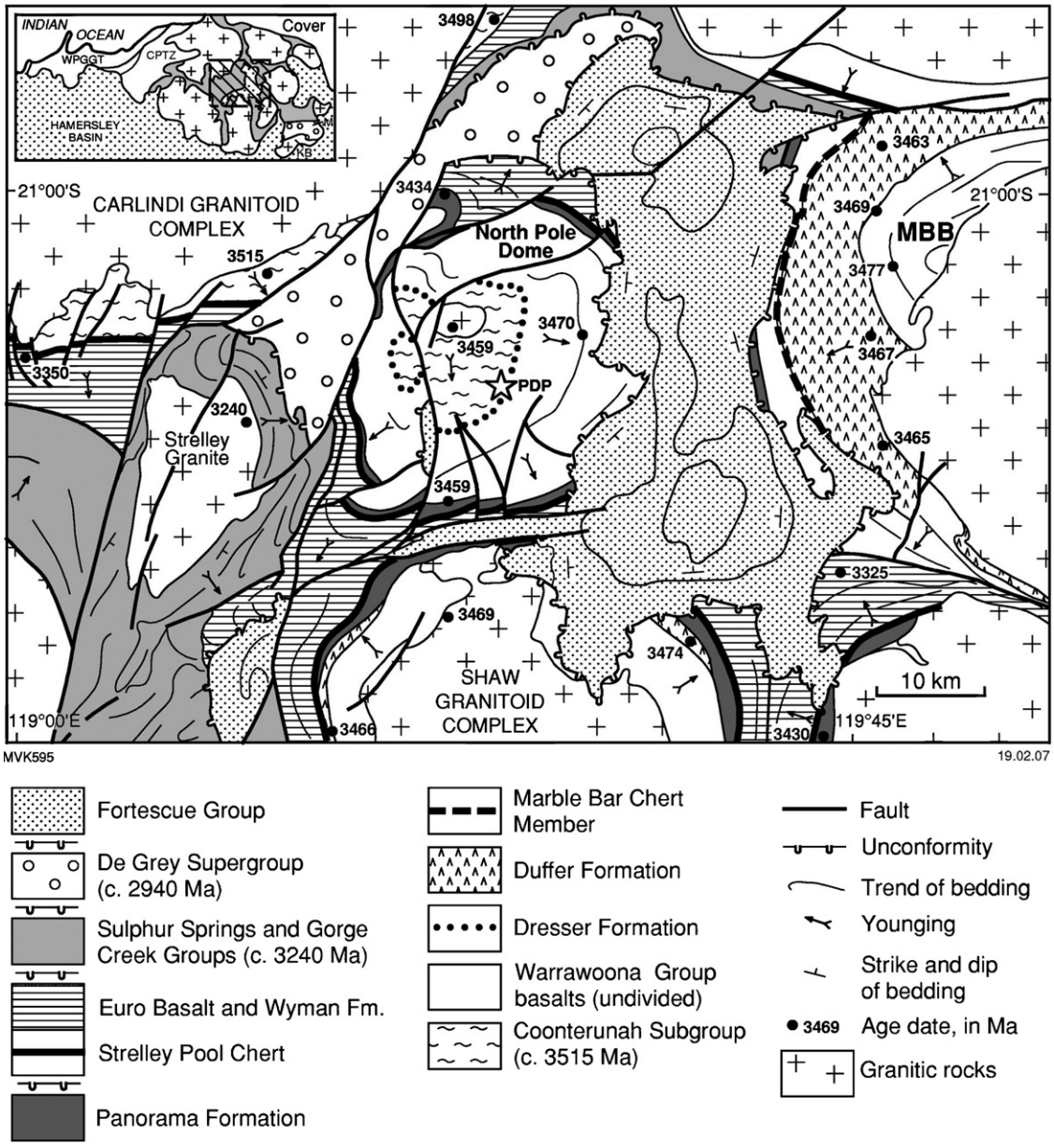

Fig. 1. Regional geology of the East Pilbara Terrane of the Pilbara Craton, showing location of drillsite PDP2.

of the Pilbara Craton, Western Australia (Fig. 1: Buick et al., 1981; Buick, 1990; Lowe, 1994). This controversy has arisen in part due to different interpretations of geological relationships, as described below, but also in part due to the effects of extreme surface weathering that, for example, is known to transform greenschist-facies ultramafic rocks into carbonates, and sedimentary carbonates and black shales into cherts (e.g., Thiry et al., 2006). This is an important factor in the current debate regarding Dresser Formation stromatolites because surface exposures of these structures are represented by either red- and black-weathering iron oxides and/or layered chert, both of which may potentially mask the original protolith material and thus limit a confident interpretation of these structures. Similar debate has arisen concerning the protolith of layered chert, the main host rock to these putative fossils, which has been interpreted as either primary silica deposits from a hot Archean ocean (e.g., Knauth and Lowe, 2003), or as primary carbonates affected by later silicification either due to Archean hydrothermal alteration (Van Kranendonk, 2006) and/or Cenozoic weathering (e.g., van de Graaff, 1983; Thiry et al., 2006).

This paper describes the geological and mineralogical features of the Dresser Formation, based on detailed examination of surface exposures and of rock samples collected from below the zone of oxidative weathering by diamond drilling in 2004, as part of a joint scientific research project between the Institute de Physique du Globe de Paris and the Geological Survey of Western Australia (Van Kranendonk et al., 2006b). Our main objective is to present detailed descriptions of the geology as a means of deciphering the geological environment of deposition and as a prerequisite for exploring potential links between sediment deposition, hydrothermal fluids and seawater circulation, mineral crystallization, metamorphism, and the development of the earliest ecological niches. Philippot et al. (2007) provided a detailed report of the isotopic results from the drillcore material.

2. Geological setting

The Dresser Formation is a ca. 3.5 Ga package of interbedded chert ± barite units and pillow basalt within the lower part of the ca. 3.52–3.42 Ga Warrawoona Group of the Pilbara Supergroup (Fig. 1: Thorpe et al., 1992b; Van Kranendonk, 2000, 2006; Van Kranendonk et al., 2006a). Exposed in the North Pole Dome, the Dresser Formation is preserved as a ring of hills, up to 14 km in diameter, and dips shallowly away from the younger, ca. 3.46 Ga North Pole Monzogranite that was emplaced into the core of the dome as a subvolcanic laccolith during eruption of the overlying, ca. 3.46–3.42 Ga, Panorama Formation (Fig. 2: Van Kranendonk, 2000; Van Kranendonk et al., 2002, 2007; Blewett et al., 2004).

The fossiliferous, bedded chert–barite unit at the base of the Dresser Formation varies between 4 and 60 m thick. It is composed of predominantly bedded grey, white, black and locally red chert, thick units of coarsely crystalline barite in layers sometimes metres thick and oriented parallel, or discordant, to bedding, conglomerate, sandstone, carbonate, and stromatolitic laminates (Lambert et al., 1978; Walter et al., 1980; Groves et al., 1981; Hickman, 1983; Buick and Dunlop, 1990; Nijman et al., 1998; Van Kranendonk, 2000, 2006). It is overlain by pillowed komatiitic basalt affected by greenschist-facies metamorphism, and underlain by spinifex-textured metabasalt that is pervasively affected by intense hydrothermal alteration and transected by hundred of veins – varying from centimetres to kilometres long – of black silica, grey silica, silica + barite, and barite, all with variable amounts of pyrite (Hickman, 1973, 1983; Van Kranendonk, 2000, 2006; Ueno et al., 2001b, 2004; Van Kranendonk and Pirajno, 2004).

A Pb–Pb isochron age of 3490 Ma was obtained from galena in barite of the chert–barite unit at North Pole (Thorpe et al., 1992b). Overlying volcanics and related intrusions in the North Pole Dome have been dated at between 3458 and 3440 Ma (Thorpe et al., 1992a; Amelin et al., 2000). Older rocks of the ca. 3515–3498 Ma Coonterunah Subgroup (Van Kranendonk et al., 2006a) crop out just to the northwest of the North Pole Dome and detrital zircons of this age have been recorded from stratigraphic intervals higher up in the North Pole Dome stratigraphy (Buick et al., 1995).

Regional mapping studies suggested that metamorphic grade in the dome was part of regional prehnite–pumpellyite to greenschist metamorphism that arose from the widespread emplacement of granitic rocks at ca. 3.3 Ga (Hickman, 1983). However, Terabayashi et al. (2003) clearly showed that metamorphic grade decreased with stratigraphic height within a number of several-kilometre-thick basalt–chert packages within the North Pole Dome stratigraphy. Whereas these authors interpreted this relationship as due to thrust stacking of oceanic crustal slices, others have provided compelling regional stratigraphic, geochemical and geochronological evidence that this was not the case (Van Kranendonk and Pirajno, 2004; Brown et al., 2006; Van Kranendonk, 2006; Smithies et al., 2005, 2007; Van Kranendonk et al., 2007). Rather, it has been suggested that this style of metamorphism resulted from repeated episodes of hydrothermal circulation within magmatically accreted volcanic packages that were bound

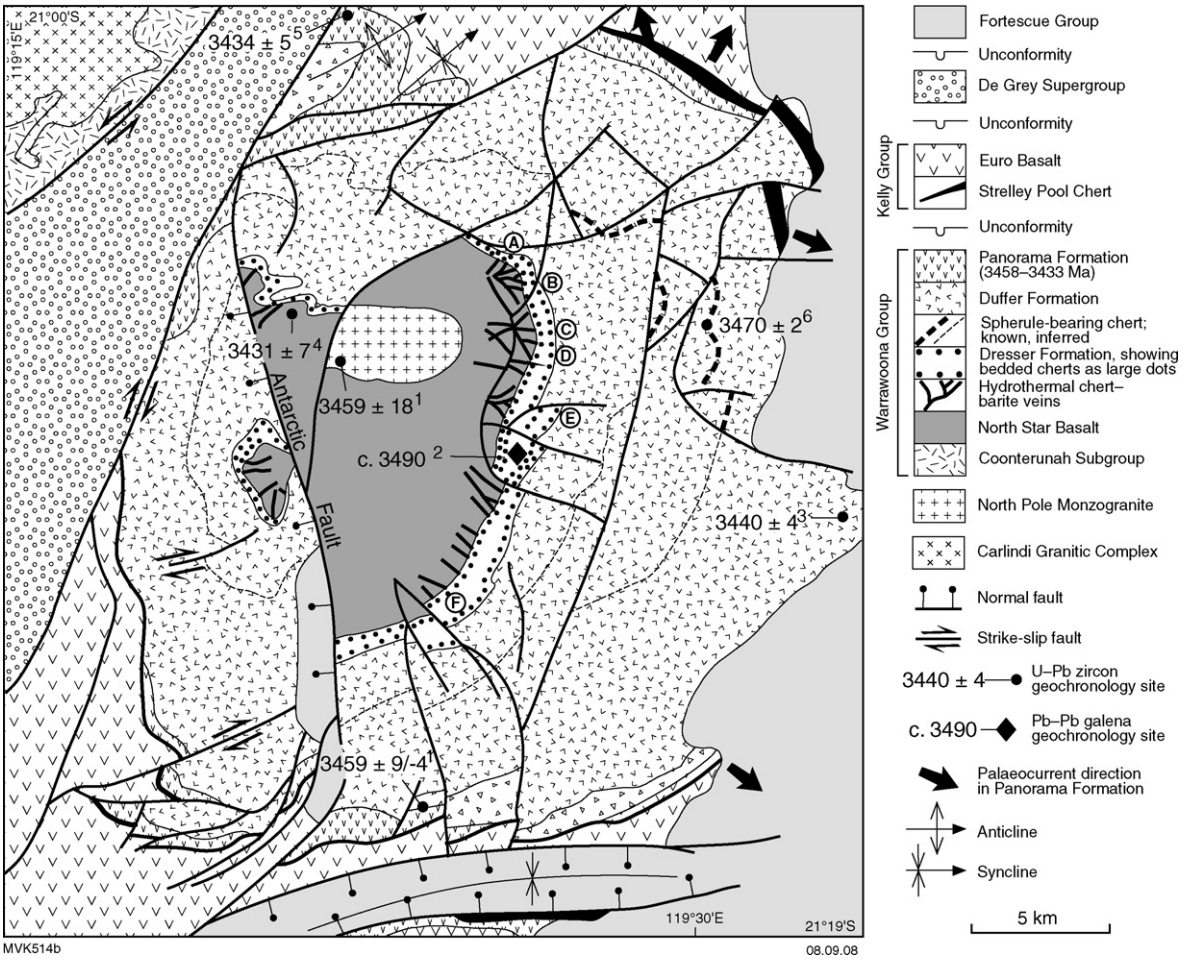

Fig. 2. Geological map of the North Pole Dome, showing the location of available age data and stratigraphic sections discussed in the text (A–F): note that location of section F is the locality of the PDP2 drillsite.

above and below by silicified sediments that acted as aquacludes to fluid circulation across package boundaries (cf. Van Kranendonk, 2006). Van Kranendonk and Pirajno (2004) and Brown et al. (2006) documented the effects of hydrothermal alteration at the level of the Dresser Formation and at other stratigraphic levels throughout the Warrawoona Group, and showed that low-temperature hydrothermal products such as hydrothermal kaolinite were locally preserved. Van Kranendonk (2000) and Brown et al. (2006) identified an amphibolite-facies metamorphic aureole around the North Pole Monzogranite in the core of the dome relating to the intrusion of this younger pluton.

2.1. Previous models of deposition

Three models have been proposed for the setting of the lowermost chert–barite unit of the Dresser Formation. One model – herein referred to as the quiet lagoon model – suggests that the rocks were deposited as bedded carbonate–gypsum evaporites and mafic volcanogenic sediments in a quiet, shallow water marine lagoon separated from the open ocean by a sand bar, following analogy with Shark Bay, Western Australia, where large and diverse living stromatolites are found today (Groves et al., 1981; Buick and Dunlop, 1990). In this model, bedded red and white chert units were interpreted as silicified carbonates and bedded barite units as seafloor evaporative gypsum deposits that were replaced by barite during later periods of hydrothermal fluid circulation. The extensive network of silica ± barite veins that underlie the formation were interpreted as the product of fluid circulation during much later events, possibly related to structural doming (e.g., Hickman, 1983), or rifting at 2.7 Ga during deposition of the Fortescue Group (cf. Buick, 1984, 1988).

Buick and Dunlop (1990) recognised up to 22 sedimentary lithofacies, of which 6 are partly or wholly chemical in origin. Lithofacies were divided into four facies assemblages, including a lower arenaceous assemblage of dominantly volcanogenic sand, one or more horizons of volcanogenic mud, a carbonate facies, and a sulfate facies. These authors contend that original carbonate mineralogy is largely replaced by cherts and pseudomorphed by sulfates, including gypsum and barite.

A second model suggests that the stromatolitic chert–barite units were deposited on oceanic crust during off-axis hydrothermal circulation and that the North Pole stratigraphy represents a set of thrust-bound ophiolite slices (Kitajima et al., 2001a,b; Terabayashi et al., 2003). Evidence presented in support of this model include (1) an interpretation of alteration styles of North Pole greenstones as equivalent to those at mid-ocean ridges (Kitajima et al., 2001a); (2) observations of repeated sections of crust with downward-increasing metamorphic temperatures across major bedded chert horizons (Terabayashi et al., 2003); (3) evidence for local fault-repetition of stratigraphy in the northern part of the dome (Ueno et al., 2001b). In this model, thrusts are interpreted as almost exclusively parallel to bedding and transported slices of oceanic crust across the tops of bedded chert horizons.

A third model suggests that the protoliths of the chert–barite unit were deposited during hydrothermal circulation in a volcanic caldera (Nijman et al., 1998; Ueno et al., 2001b; Van Kranendonk et al., 2001; Van Kranendonk, 2006, 2007), possibly during regional crustal extension (Nijman and de Vries, 2004). In this model, the silica ± barite veins that underlie the bedded chert-carbonate units are interpreted as fossil hydrothermal fluid pathways that formed synchronously with, and were the cause of, deposition of the bedded chert–barite units. Hydrothermal fluid flow was accompanied by extensive hydrothermal alteration of the footwall, with characteristic assemblages and zonation indicative of a steam-heated acid–sulfate hydrothermal system under shallow water conditions (Van Kranendonk and Pirajno, 2004; Van Kranendonk, 2006). Evidence was presented for silica- and barite-rich fluid circulation and resultant precipitation of chert and barite during episodic periods of growth faulting, with hydrothermal fluids penetrating to the surface along growth faults (Nijman et al., 1998). Growth faulting was accompanied by soft-sediment deformation (Van Kranendonk, 2006).

Nijman et al. (1998) proposed a three tier depositional system for the lower chert–barite unit of the Dresser Formation, starting with a regressive shoaling-upwards basal sheet that corresponds to uplift, faulting and fracturing of the basalt footwall. Felsic volcanism commenced at this time, followed by a tidal deltaic deposystem with considerable volcaniclastic influx. Normal faulting and hydrothermal activity accompanied this stage. A thin unit of overlying sandstone is interpreted as tier three, representing a transgressive sand sheet deposited during a return to deeper water conditions. Support for this model comes from the discovery of coarse conglomerates with barite clasts at several levels within the accumulating sedimentary pile, and from the presence of large (>100 m^2) barite mounds onlapped by bedded chert units (Nijman et al., 1998). Further support for a hydrothermal model was provided by geological evidence of multiple sets of chert and barite veins disconformably overlain by sandstone, of barite blocks overlain by bedded chert, of hydrothermal kaolinite in chert veins, and an extensive area of intense hydrothermal alteration (including acid–sulfate alteration) that has affected footwall rocks beneath the bedded chert–barite units, but not the overlying rocks (Ueno et al., 2001b; Van Kranendonk and Pirajno, 2004; Pirajno and Van Kranendonk, 2005; Van Kranendonk, 2006). These authors provided clear evidence that hydrothermal activity occurred during accumulation of the sedimentary pile in the form of syn-depositional hydrothermal breccias and footwall alteration. Furthermore, Van Kranendonk (2006) suggested that stromatolites may have grown at, and even possibly within, the mouths of hydrothermal vents, and this was used as evidence to suggest that at least some stromatolites in the Dresser Formation were built by communities of chemoautotrophs.

2.2. Biogenicity of fossils

Debate continues over the biogenicity of putative stromatolites and microfossils in the Dresser Formation and at various other levels in the Pilbara Supergroup. Fossil stromatolites in the Dresser Formation include domical and stratiform varieties with wrinkly laminations, and coniform stromatolites in chert with well-defined bedding, including ripples. These structures have been variably interpreted as stromatolites (Walter et al., 1980; Groves et al., 1981; Walter, 1983; Van Kranendonk, 2000, 2006), stromatoloids, or probable or possible stromatolites (Buick et al., 1981), or even abiological structures resulting from deformation (Lowe, 1994). More convincing evidence of diverse stromatolites has been described from the unconformably overlying Strelley Pool Chert within the North Pole Dome (Hofmann et al., 1999; Van Kranendonk et al., 2001; Allwood et al., 2006; Van Kranendonk, 2006, 2007).

Carbonaceous spheroids were described by Dunlop et al. (1978) and interpreted as microfossils, although Buick (1990) offered caution. Filamentous microfossils were described by Awramik et al. (1983, 1988), Schopf (1993) and Schopf et al. (2002, 2007) at other sites within the East Pilbara, but these have been contested (Buick, 1984, 1988; Brasier et al., 2002, 2004). Carbonaceous filaments with $\delta^{13}C$ values of −35‰ have been described from silica veins that underlie the bedded chert–barite units and have been interpreted as microfossils of chemoautotrophs (Ueno et al., 2001a,b, 2004, 2006). However, the biogenicity of such structures has been challenged on several grounds, including morphology (Brasier et

al., 2002, 2004), abiological synthesis of biomorphs that have an uncanny resemblance to some of the putative microfossils (Garcia-Ruiz et al., 2003), and the possibility of abiogenic synthesis of organic compounds (e.g., McCollom, 2003; Lindsay et al., 2005).

3. Methods

Geological mapping was undertaken of surface outcrops of the Dresser Formation in order to best assess where to locate the drillsite, in a reasonably accessible area, away from faulting and overabundant hydrothermal veining, and where a representative stratigraphic section was preserved. Several geological sections were made through the formation at various places along strike, including three closely spaced sections at the drillsite.

Based on these criteria, a site was chosen in the southeastern part of the North Pole Dome (Fig. 2), where bedded sedimentary rocks of the Dresser Formation dip 40° south-southeast between weakly metamorphosed pillow basalts. Three closely spaced drillholes were attempted to the south of the surface outcrops, in the stratigraphic hangingwall, and were oriented at 50° → 330° in order to intersect the bedding at right angles (Table 1). The first hole (PDP2a), located closest to the outcrops of bedded sedimentary rock, was drilled with HQ core (75.7 mm diameter) to a depth of 50.6 m through pillowed metabasalt affected by heavy surficial weathering, at which depth the hole was abandoned. No analysis of this core has been made. The second hole (PDP2b) was located further away from the surface outcrops and drilled through metabasalt by RC hammer to a depth of 84.0 m, when red flakes of jaspilitic chert emerged from the hole. Diamond drilling with NQ core (47.6 mm diameter) commenced at this depth and continued from 84.0 to 109.6 m, through the bedded sedimentary rocks, into the underlying metabasalt. The third hole (PDP2c) was sited 14 m further to the south-southeast. Knowing the depth of weathering from the PDP2b and the dip and continuity of the bedded sedimentary rocks, the first 69.3 m of this hole was drilled by RC hammer to penetrate below the zone of weathering but remain within the overlying metabasalts. From there, drilling continued by NQ diamond drillcore. Metabasalt was intersected to a depth of 92.3 m, where the upper contact of the bedded sedimentary rocks was intersected. Diamond drilling was continued through the chert–barite unit to a depth of 114.6 m, well into the underlying basalt.

Polished thin sections and doubly polished thin sections were made of all representative units and textures observed in the drillcore material. The thin section textural observations presented herein come mainly from thin sections of core from PDP2c, since it transected the most units of interest, but samples from PDP2b are also described.

Drillcore from PDP2c was analysed using Hyperspectral mineralogical logging (the HyLogging System) developed by the CSIRO, based on very high-resolution digital imaging of the core and spectroscopic determination of mineralogy using automated interpretation software (The Spectral Geologist (TSG)™). Results are presented in Van Kranendonk et al. (2006b).

4. Results

4.1. Surface geology at the drillsite

Surface outcrops at the drillsite locality indicate that the lowermost chert–barite unit of the Dresser Formation varies between 6 and 12 m thick across 10's of metres of strike length (Fig. 3). Exposures continue for kilometres along strike to either side of the drillsite, but were not mapped in detail. However, it was observed

Table 1
Drillhole data for the PDP project

Drillhole number	Direction (plunge→ azimuth)	Surface location (in GDA co-ordinates): Grid Zone; Easting; Northing	Surface location: latitude; longitude	Interval drilled with HQ core (m)	Interval drilled by RC hammer (m)	Interval drilled with NQ core (m)	True vertical depth at end of hole (m)
PDP2a	50° → 330°	50K; 0752229E; 7656300N	21°10′33″S; 119°25′50″E	0–50.6			38.8
PDP2b	50° → 330°	50K; 0752249E; 7656267N	21°10′34″S; 119°25′50.9″E		0–84.0	84.0–109.6	84.0
PDP2c	50° → 330°	50K; 0752253E; 7656259N	21°10′34.4″S; 119° 25′51″E		0–69.3	69.3–114.6	87.8

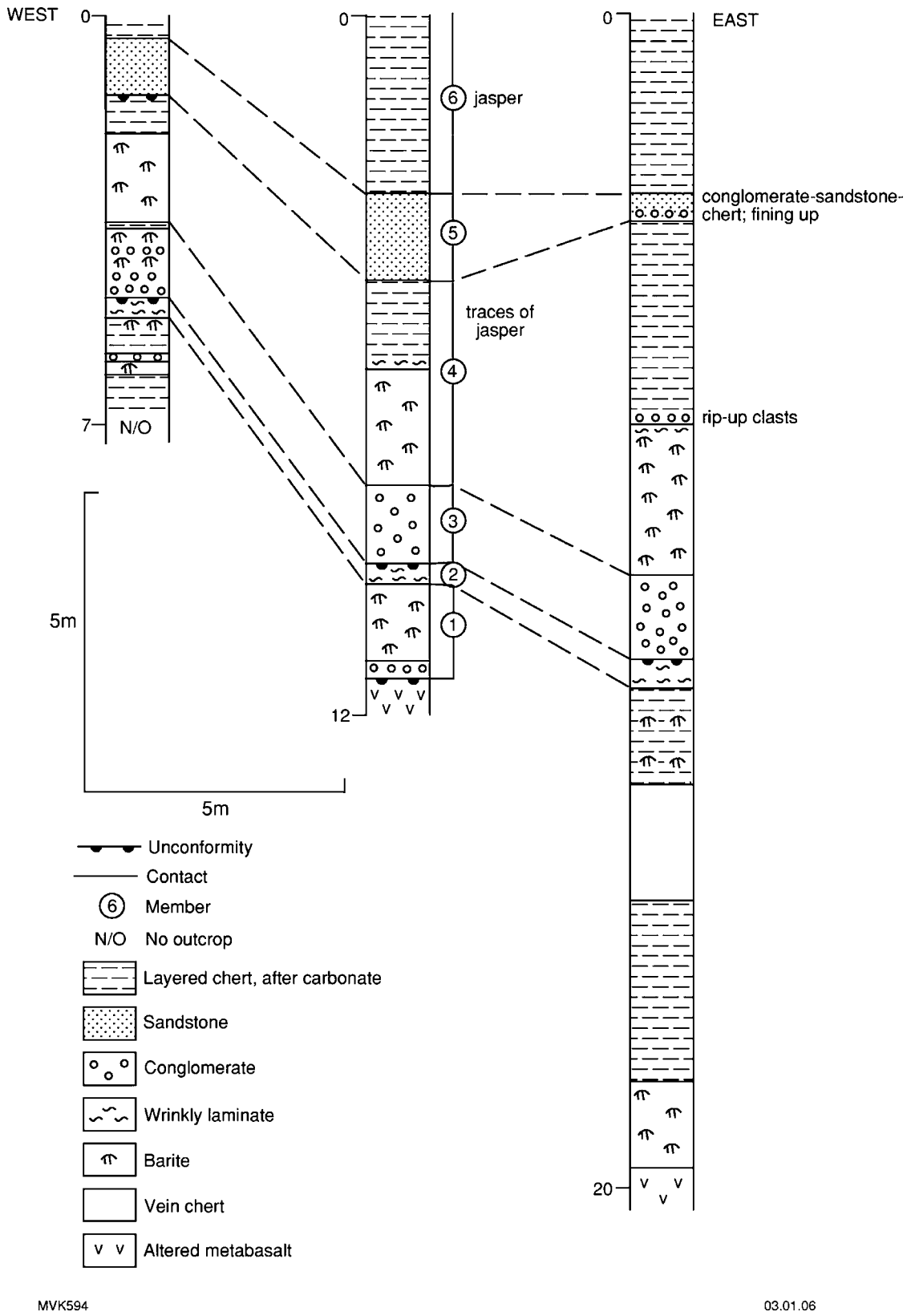

Fig. 3. Stratigraphic sections from along strike surface exposures of the lower chert–barite unit of the Dresser Formation at the PDP2 drillsite locality, showing variations in the thicknesses of members.

that lateral thickness and facies variations occur over 100's of metres along strike, across growth faults (see also Nijman et al., 1998). Underlying the chert–barite unit is pale green, carbonate-altered, metakomatiitic basalt that is transected by numerous veins of grey to black silica and veins of silica + barite. Overlying the chert–barite unit is dark-green, chlorite–carbonate-altered pillow basalt that contains a variety of well-preserved primary volcanic textures including amygdales, varioles, and abundant interpillow hyaloclastite breccia. As elsewhere in the formation, a significant observation is that not a single vein of silica ± barite cuts the overlying basalts (Van Kranendonk, 2000).

Bedded sedimentary rocks of the lowermost chert–barite unit of the Dresser Formation can be divided into six members (Fig. 3). Member 1 at the base has a locally exposed basal contact with underlying basalts that includes a 2 cm thick unit of angular sandstone to flat pebble conglomerate with clasts of metabasalt

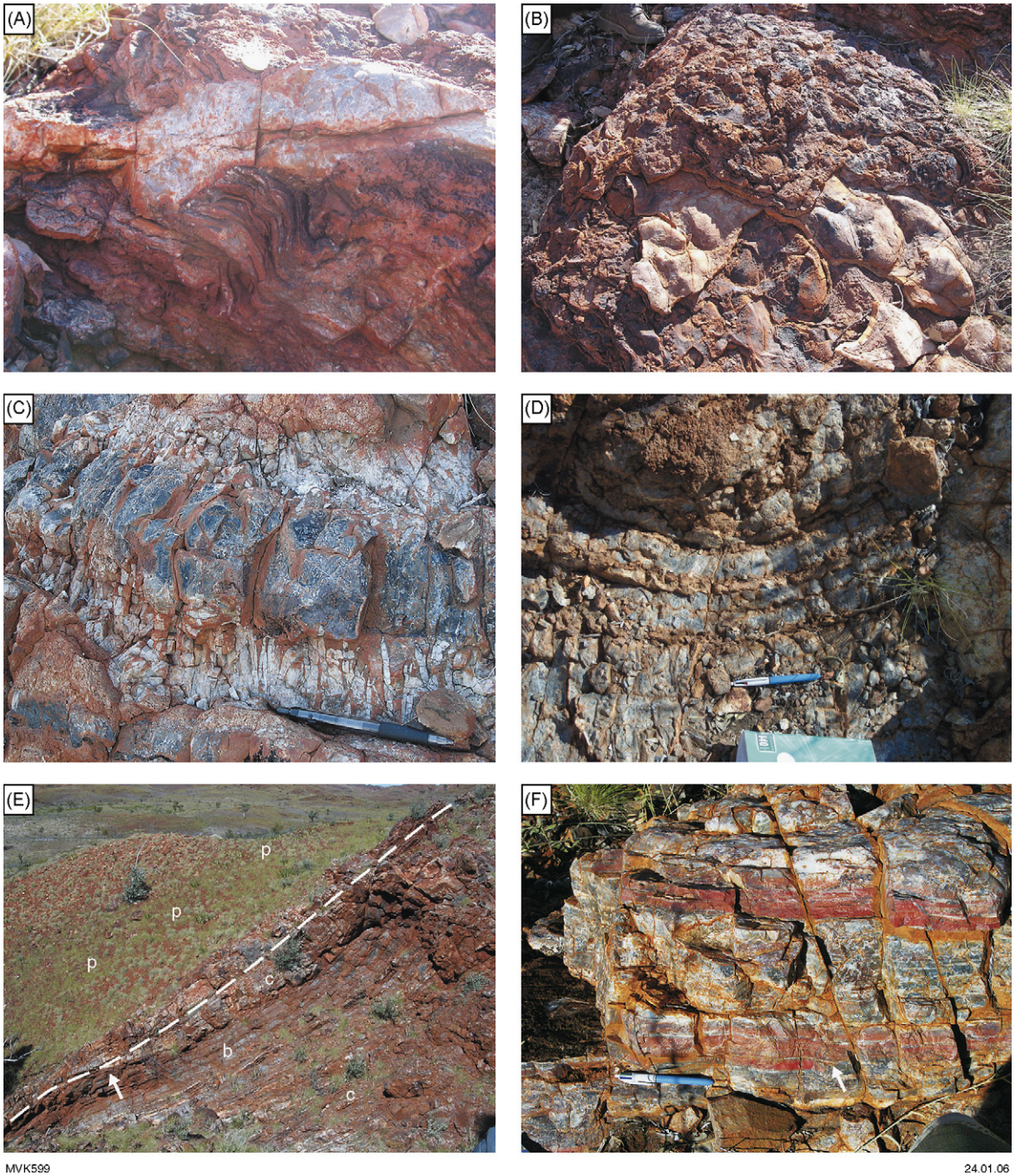

Fig. 4. Surface outcrop features of the lower chert–barite unit of the Dresser Formation at the drillsite: (A) cross-sectional view of wrinkly stratiform stromatolite, cut by a grey silica vein that is ~15 cm wide; (B) view looking down onto a bedding surface of wrinkly stratiform stromatolite: pale, smooth textured rock is bedding-parallel sheet of hydrothermal chert (width of view ~50 cm); (C) zoned barite–chert vein cutting diamictite of member 3; (D) a thick sheet composed of alternating layers of coarsely crystalline barite and chert, subparallel to bedding, which was emplaced through multiple crack-seal episodes of hydrothermal fluid circulation; (E) view, looking south-southwest, of the angular unconformity (dashed line and arrow) between underlying chert (c) and barite (b) of member 4, and overlying sandstone and layered chert of members 5 and 6: rubbly hill above and left of chert is broken outcrop of overlying pillow basalt (p) (layered cherty rocks ~3 m thick); (F) jaspilitic chert of member 6, showing the discontinuous nature of jasper in the bands (arrow).

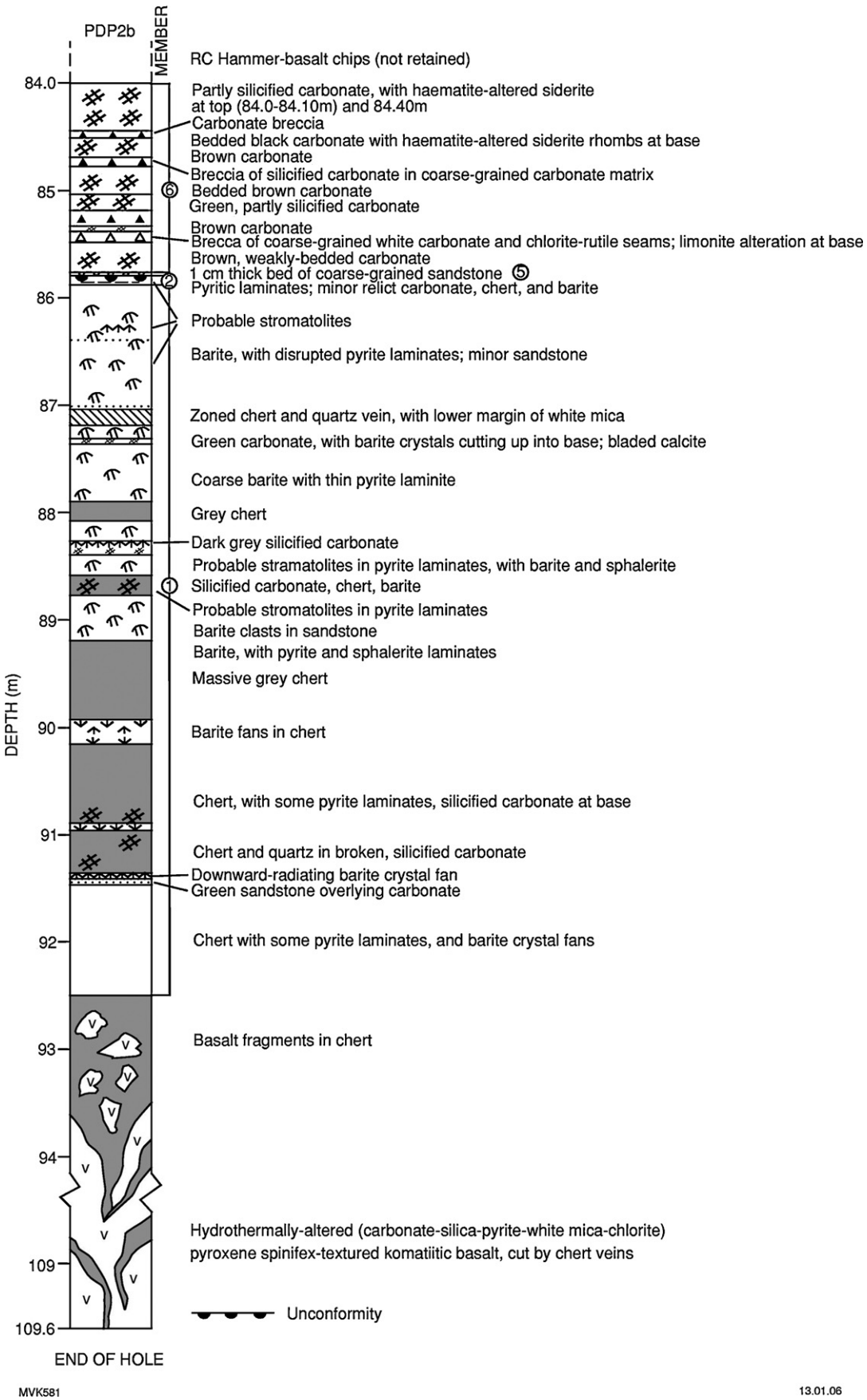

Fig. 5. Stratigraphic log of drillhole PDP2b.

up to 1 cm large. Elsewhere, the lower contact of member 1 is intruded either by black silica and/or coarsely crystalline barite veins. The remainder of member 1 consists of coarsely crystalline stratiform barite that is interbedded with greenish-grey, silicified, fine-grained sedimentary rock and thin layers of finely bedded wrinkly laminate.

Conformably overlying member 1 is 30–40 cm of black-weathering wrinkly laminate of member 2 that contains abundant,

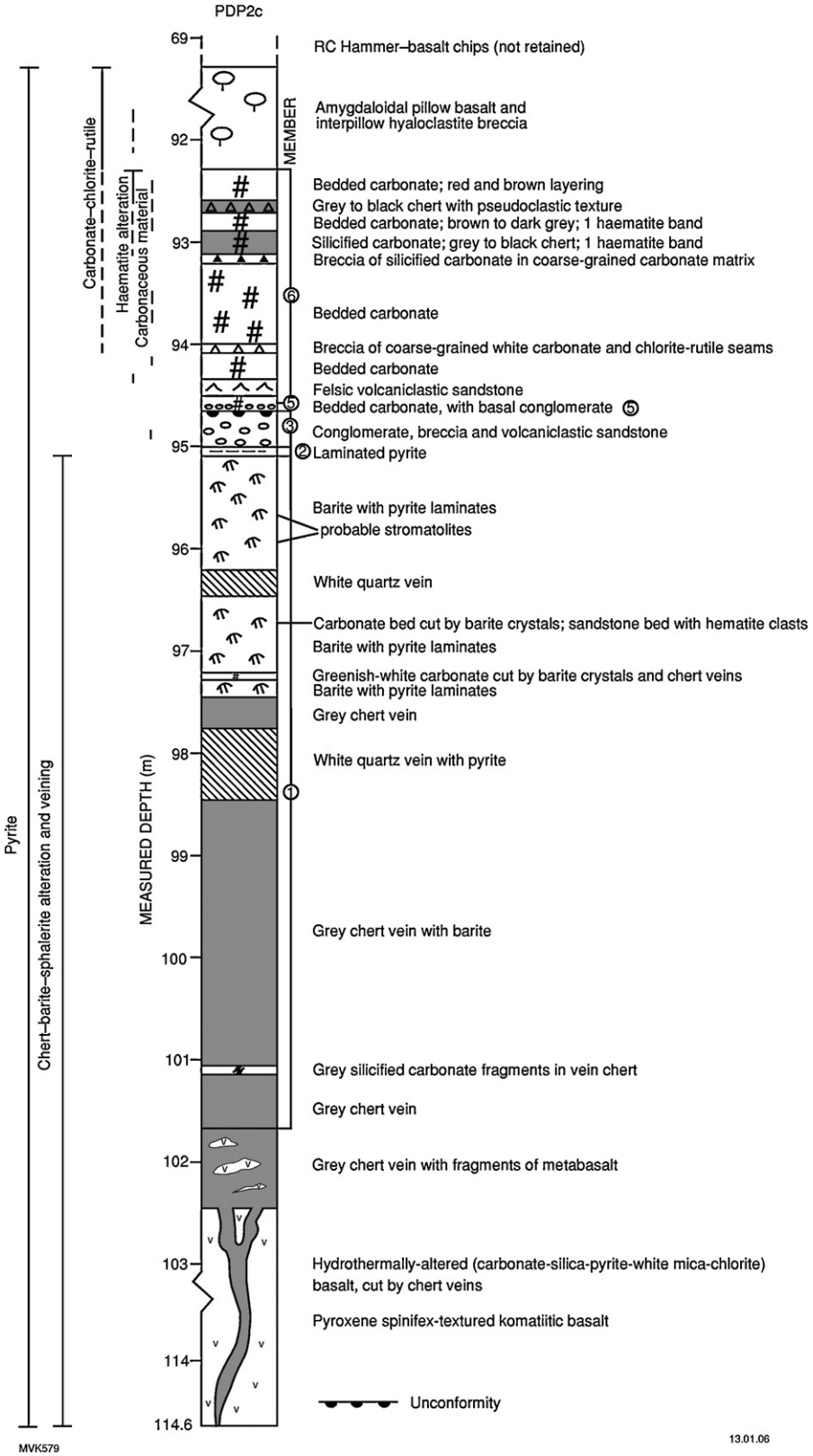

Fig. 6. Stratigraphic log of drillhole PDP2c, showing alteration mineral assemblages.

low-amplitude domical shapes that are interpreted as probable stratiform to domical stromatolites (Fig. 4A and B).

Overlying member 2, locally with a downcutting erosional lower contact, is a ~150 cm thick unit of creamy white-weathering conglomerate and sandstone (member 3). This unit contains clasts, to 2 cm large, of wrinkly laminates and chert, but shows no internal bedding. This member is locally cut by discordant chert and barite veins near the base of the unit (Fig. 4C), and by 20–30 cm wide, coarsely crystalline barite veins oriented parallel to bedding towards the top of the unit. A 10 cm bed of white-weathering, fine-

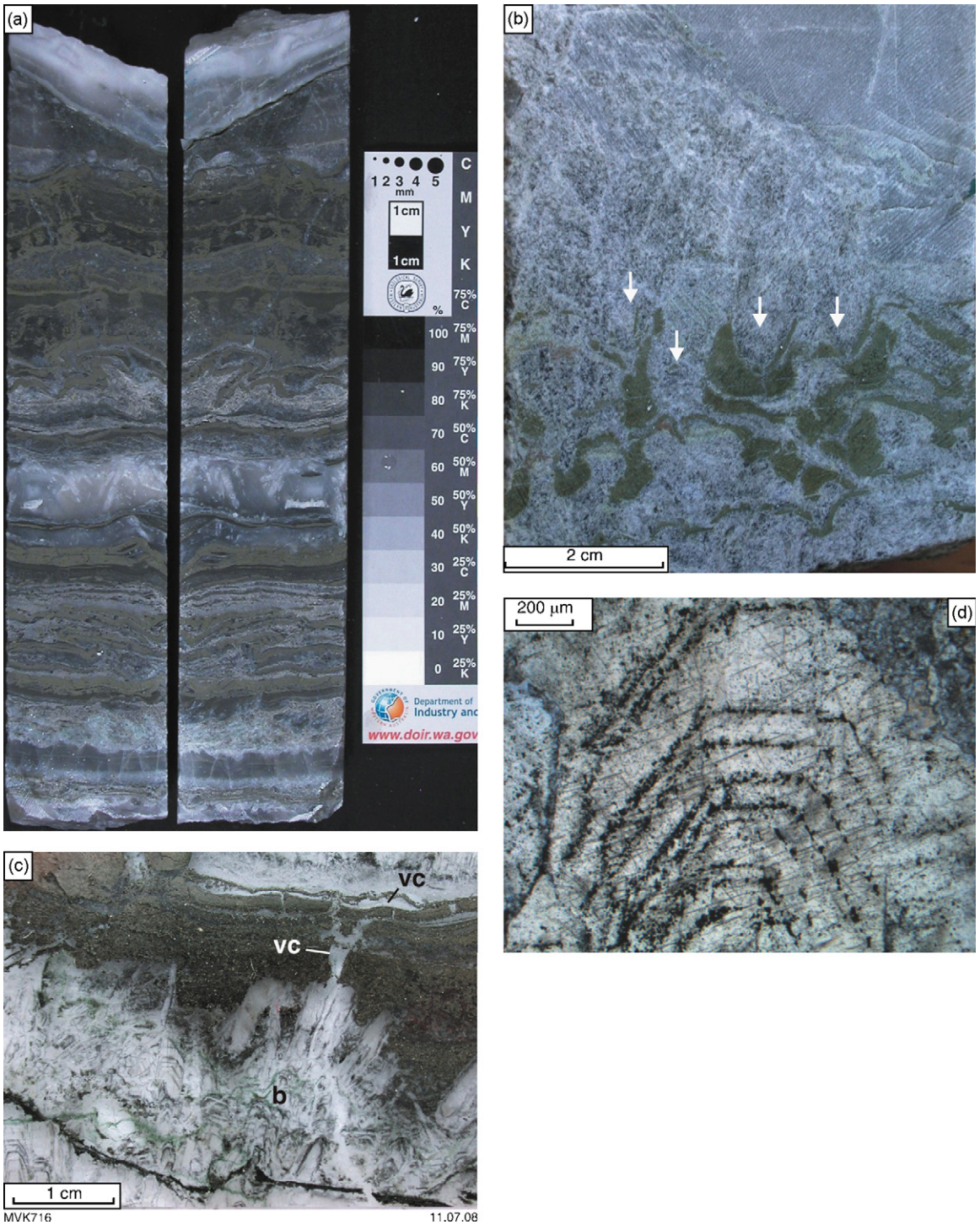

Fig. 7. Features of pyritic laminates and barite from member 1 in drillcore: (a) section of core (88.4–88.6 m in PDP2b), showing the repeated, alternating nature of barite crystals and pyrite laminates in member 1 and soft-sediment deformation of pyrite laminates. Note the variety of styles of the pyritic laminates, including flat laminates on carbonate at base, irregular laminates partway up, laminates with stromatolitic forms near the top, and flat laminates at the top; (b) section of drillcore showing upward-radiating and downward-radiating sets of barite crystals intrusive into pyritic laminates (from 88.9 m depth in PDP2b); (c) plane light, whole thin section view of carbonate and pyrite laminates cut by barite crystals: note the progressive excision of layering by lower barite from right to left, the well-developed pyritic growth zones in lower barite (b), and thin, subhorizontal layers of chert–barite in pyritic laminates that are fed by a cross-cutting silica vein (vc); (d) pyrite growth zones in barite crystal (88.4 m depth in PDP2b).

to medium-grained sandstone occurs at the top of the unit, which may represent a felsic volcaniclastic rock, but is too weathered in outcrop to be certain.

The bottom part of member 4 is composed of 10 cm thick layers of brown carbonate and metre-thick layers of coarsely crystalline stratiform barite (crystals to 30 cm long: Fig. 4D). Wrinkly laminates occur towards the top of the thick barite units. The top part of this member is composed of 70–160 cm thick of centimetre-layered brown, grey, white, and black chert, with very thin wrinkly laminates at the base, and one broadly domical, low-amplitude stromatolite (30 cm wide × 5 cm high) in the middle. At the easternmost outcrops, the transition from wrinkly laminate and barite to overlying layered chert is marked by a 10 cm thick unit of rip-up conglomerate with 1 cm clasts of wrinkly laminates.

Member 5 disconformably to unconformably overlies member 4 (Figs. 3 and 4E) and mostly consists of fairly homogeneous greenish-grey, medium-grained sandstone with only faint traces of bedding. At the easternmost outcrops, the member consists of a 50 cm thick fining upwards sequence of conglomerate–sandstone–chert.

Member 6 conformably overlies member 5 and is up to 7 m thick. It consists of centimetre-layered grey, white, and red layered chert (Fig. 4F).

4.2. Geology of the drillcore

In drillhole sections PDP2b and PDP2c, bedded sedimentary rocks are between 8.5 and 9.0 m thick (Figs. 5 and 6). Neither core contains all six of the members identified in outcrop; members 3 and 4 are missing in PDP2b, and member 4 is missing in PDP2c. The downcutting unconformity at the base of member 5 is interpreted to be the cause of the loss of member 4 in both drillholes and the significant thinning of member 3 in PDP2b, whereas the significant thinning of member 5 in PDP2b is interpreted to be the result of a lateral facies change. Units in the drillcore are described below, from stratigraphic base to top.

4.2.1. Underlying basalt

The underlying komatiitic basalt preserves relict pyroxene spinifex texture that is now completely replaced by a carbonate-white mica–pyrite assemblage, with leucoxene mantling igneous ilmenite. Paragonite (Na-rich mica) has been identified over a 1 m interval by Hyperspectral analysis of the core. Vesicles are filled by an early phase of carbonate and a subsequent assemblage of microquartz, recrystallized carbonate rhombs and white mica that was introduced by cross-cutting veins. These veins at least locally consist of two distinct phases: (1) an early phase of black chert composed of microquartz, recrystallized carbonate rhombs, abundant carbonaceous material and minor pyrite with a remarkable pseudoclastic texture of rounded clasts of variable size in a slightly paler matrix; (2) a later phase of white microquartz with radiating fibrous quartz texture and with zones of carbonate rhombs or scattered carbonate rhombs in the microquartz.

4.2.2. Member 1

Member 1 consists of 255–530 cm of dominantly coarse crystalline barite, with centimetre-thick beds of finely laminated pyrite ± sphalerite, and variable amounts and thicknesses of zoned grey to white chert veins up to 260 cm thick. Bedded carbonate is present in this member, as well as minor amounts of sandstone, as described below.

Barite forms a variety of shapes and styles of crystal fans. Most are upward-radiating crystal sets, generally 5–15 cm thick, separated by finely laminated pyrite (FeS_2) ± sphalerite ((Zn, Fe)S) (Fig. 7a). Whereas most crystal splays are coarse from base to top, some splays grade from coarse at the base, to finer crystals at the top. Most barite splays are demonstrably intrusive into the sulfide laminates, and locally into carbonate, including downward-radiating barite crystal splays (Fig. 7b and c). However, there are examples in the core where flat sulfide laminates occur atop coarse barite crystal fans (Fig. 7a), suggesting the possibility of periodic deposition of pyrite laminates directly onto eroded barite crystals, although this is not confidently confirmed. Characteristically, the coarser, euhedral barite crystals show well-developed growth zoning. At some levels, but not everywhere, growth zones in barite are defined by fine-grained pyrite (Fig. 7d: Philippot et al., 2007).

The pyritic laminates vary widely in form from flat, finely bedded laminates, to laminates affected by soft-sediment deformation, to laminates with columnar stromatolite-like textures, to laminates with irregular shapes pushed up (or down) by barite crystal fans (Fig. 7a and b). In flat-bedded and stromatolitic pyritic laminates, the millimetre-scale layering is composed of pyrite, with subordinate carbonate, chert, barite, and sphalerite. Pyrite laminates with preserved stromatolite forms occur away from areas affected by barite crystal growth (Fig. 8a), and thus did not attain their form as the result of later crystal modification of bedding, as has been suggested for some Precambrian stromatolite-like forms (cf. Grotzinger and Rothman, 1996). In most pyritic laminates, the

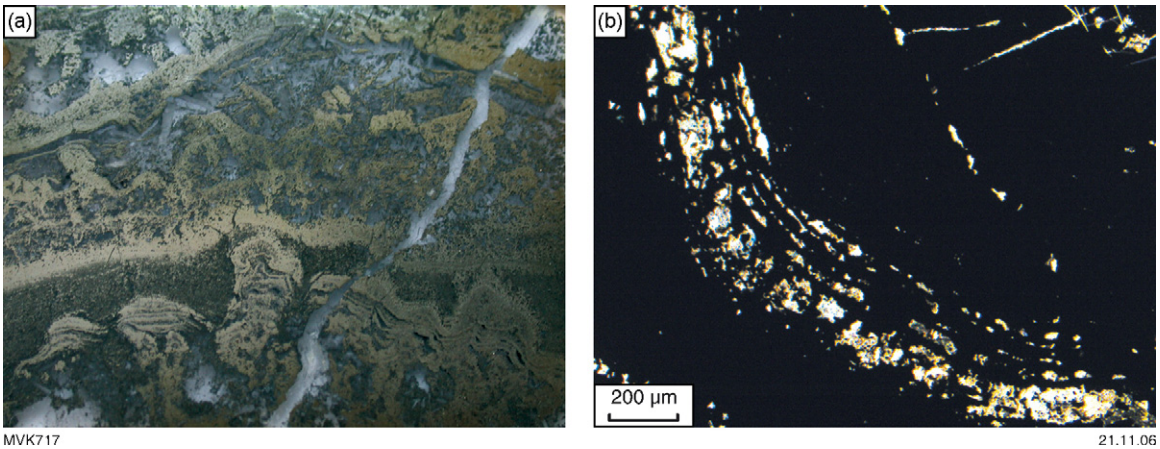

Fig. 8. (a) Whole thin section view of pyrite-replaced columnar stromatolites (88.7 m in PDP2b) (width of view ~5 cm); (B) cross-polarised thin section views of relict carbonate in replacive pyritic laminates (from 95.35 m in PDP2c): note the thin, cross-cutting veins of pyrite across the carbonate, indicating pyrite replacement of carbonate rather than carbonate replacement of pyrite.

pyrite is coarsely crystalline, and grew around and replaced former carbonate: this is also true of the columnar stromatolites (Fig. 8b). Chert, barite and sphalerite are later replacement mineral phases, as described below (see Mineral Paragenesis).

Thin carbonate and sandstone beds are locally preserved. A centimetre-thick bed of carbonate and overlying sandstone is preserved in PDP2c at 96.5 m (Fig. 9a). Here, the carbonate is green in colour and has been partly replaced by pyrite, prior to hav-

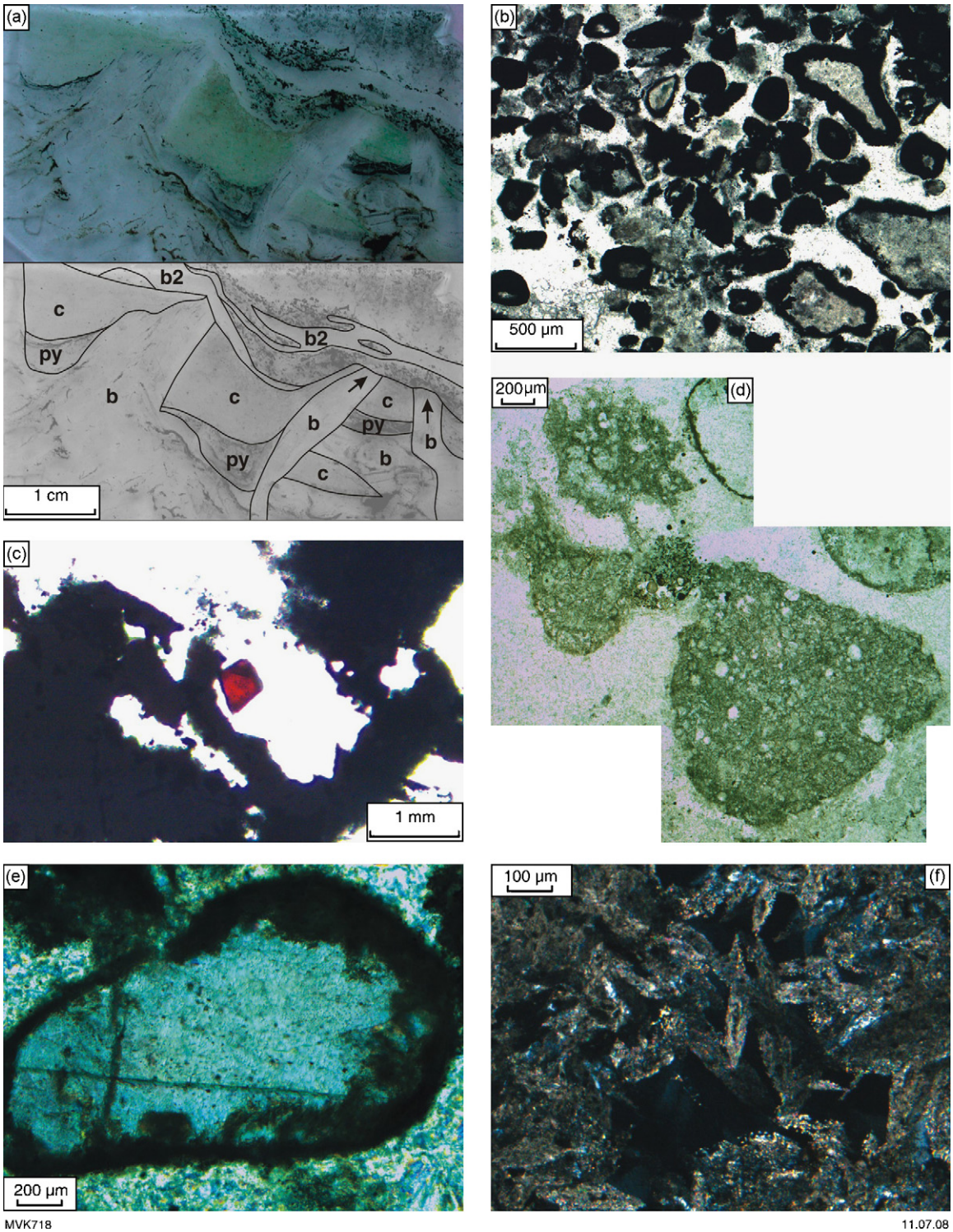

Fig. 9. (a) Whole thin section view, and interpreted line drawing, of bedded carbonate (c) that has been replaced by pyrite (py) and cut by barite crystals (b), with local sphalerite rims, prior to deposition of overlying sandstone (dotted pattern). Note the bedding-subparallel veins of barite (b2) in the overlying sandstone (96.6 m in PDP2c, as shown in Fig. 7c) and also the eroded barite crystal tops that cut the pyrite-replaced carbonate (heavy arrows in line drawing); (b) plane polarised thin section view of the sandstone from the top of (a), showing carbonate-replaced sand grains rimmed by pyrite; (c) plane polarised thin section view of the sandstone from the top of (a), showing euhedral detrital haematite crystal surrounded by replacement pyrite; (d) plane polarised thin section view of intermediate volcanic clast in sandstone from 88.8 m in PDP2b; (e) plane polarised thin section view of carbonate-altered barite clast in sandstone from 88.8 m in PDP2b; (f) cross-polarised thin section view of bladed carbonate texture in chert from 87.3 m depth in PDP2b.

ing been cut by barite crystals. These barite crystals cut right through to almost the very top of the carbonate bed. The crystals, as is typical for most of the coarse barite crystals in thin section, have a coarse crystalline core and a mantle consisting of a fine-grained intergrowth of microquartz and barite that has partly resorbed the barite crystals themselves. This marginal zone to the barite crystals continues around the crystal tops without showing any indication of thinning through erosion by the overlying sediment, indicating that the crystals did not penetrate through the top of the sediment but crystallized within the carbonate sediment. However, it is clear from the fact that the overlying sandstone thins over the tops of the barite crystals, and thickens over the troughs between crystals, that the barite crystals formed topography on the seafloor and thus were essentially synchronous with sediment accumulation and crystallized very close to the paleosurface (Fig. 9a). Supporting evidence for this also comes from outcrop examples of diagenetic barite crystal growth that deform immediately overlying sediment, but that are overlain by flat-lying sediment unaffected by crystal growth (see Fig. 11d in Van Kranendonk, 2006).

The sandstone overlying the carbonate–pyrite–barite association described above contains sand grains that are dominantly

Fig. 10. Section of drillcore PDP2c, from 94.65 to 95.05 m depth: (a) lower half, showing pyritic laminates of member 2 at base, and lower part of diamictite of member 3; (b) upper half, showing upper part of diamictite of member 3, unconformably overlying basal conglomerate of member 5, and bedded carbonates of member 6 that are partly replaced by pyrite. Note the white carbonate–pyrite vein in member 3 that is cut off by the unconformity at the base of member 5.

composed of very fine-grained carbonate rimmed by pyrite (Fig. 9b). One of the carbonate grains was observed to contain a core of microquartz, indicating carbonate replacement of protolith grains, followed by pyrite replacement. Also present are a very few (we identified three in one thin section), very fine-grained, euhedral to subhedral haematite (or haematite-replaced carbonate) grains (Fig. 9c).

Sandstone at 88.8 m in PDP2b contains well-rounded clasts, 1–3 mm large, of vesicular microlitic basalt clasts (Fig. 9d), barite, carbonate-altered barite (Fig. 9e), laminated pyrite, haematite, and haematite-altered coarse crystalline carbonate in a matrix of secondary microquartz. This sandstone bed is overlain by further intervals of laminated pyrite and barite crystal fans (Fig. 5).

Sphalerite forms zones around barite crystals, occurs in barite + silica veins that cut laminated pyrite, and is precipitated in between individual laminates of pyrite that have been forced apart by the invading siliceous and barite-rich fluids. Thus, sphalerite post-dates episodes of pyrite precipitation and is associated with the intrusion of barite veins.

Bladed calcite was observed at 87.3 m depth in PDP2b, in a matrix of microquartz (Fig. 9f).

4.2.3. Member 2

Member 2 consists of flat, thinly bedded pyritic laminates between 5 and 10 cm thick (see bottom of Fig. 10). It is not clear that they differ in any way from pyritic laminates in the underlying member, other than being slightly thicker and not intruded by coarse barite crystal fans. Pyritic laminates are cut by veins of microquartz with a barite and sphalerite core that commonly intrude parallel to bedding, precipitating sphalerite along pyrite contacts.

4.2.4. Member 3

Member 3 in PDP2c is 37 cm thick and can be divided roughly at the midway point into two subunits (Figs. 10 and 11). The lower subunit consists of numerous long, thin, disrupted clasts of laminated pyrite (Fig. 12a) and fine-grained, green carbonate in a matrix of microquartz with recrystallized euhedral carbonate rhombs. At the base and at the top of the subunit are wedges of volcaniclastic rock. The top wedge is part of a clast of medium- to coarse-grained volcaniclastic rock and fine-grained ash that is overturned, as indicated by an upward-cutting erosional contact between the ash and the volcaniclastic rock, and by downward-facing graded beds in the ash unit (top of Figs. 10a and 11). The volcaniclastic sandstone is composed of carbonate- and white mica-altered volcanic clasts that consist mostly of intermediate to felsic volcanic rock fragments. Most clasts are fine-grained (devitrified volcanic glass), but some are plagioclase porphyritic (Fig. 12b), and others have small vesicles. Although the geochemical composition of the clasts has not been determined analytically, the fine-grained felsic composition of the clasts suggests a felsic to intermediate, rather than a mafic volcanic protolith.

The overlying subunit contains a 2–3 cm thick basal bed of fining upward, coarse- to fine-grained volcaniclastic rock and welded tuff. The base of this bed is poorly sorted pebbly sandstone (Figs. 10 and 11) with well rounded to subangular clasts, up

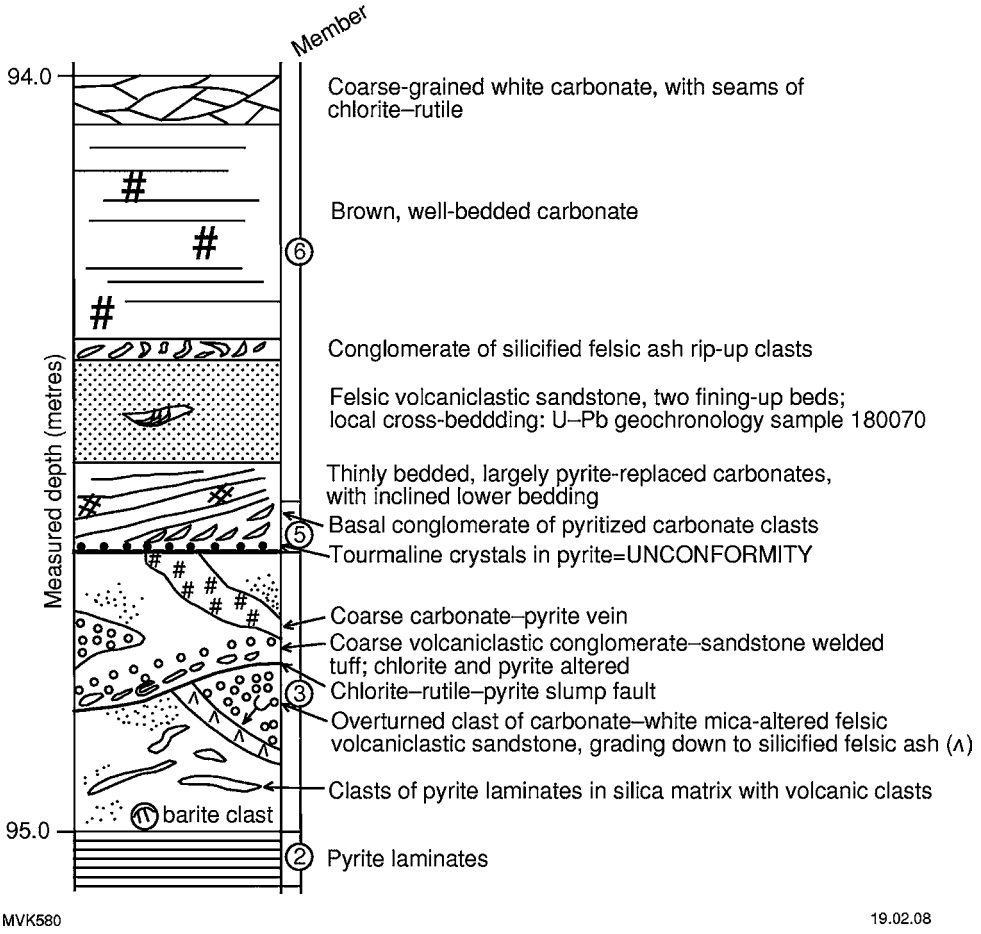

Fig. 11. Detailed interpretative geological log of part of drillcore PDP2c, from 94.0 to 95.05 m depth, corresponding to the drillcore shown in Fig. 10.

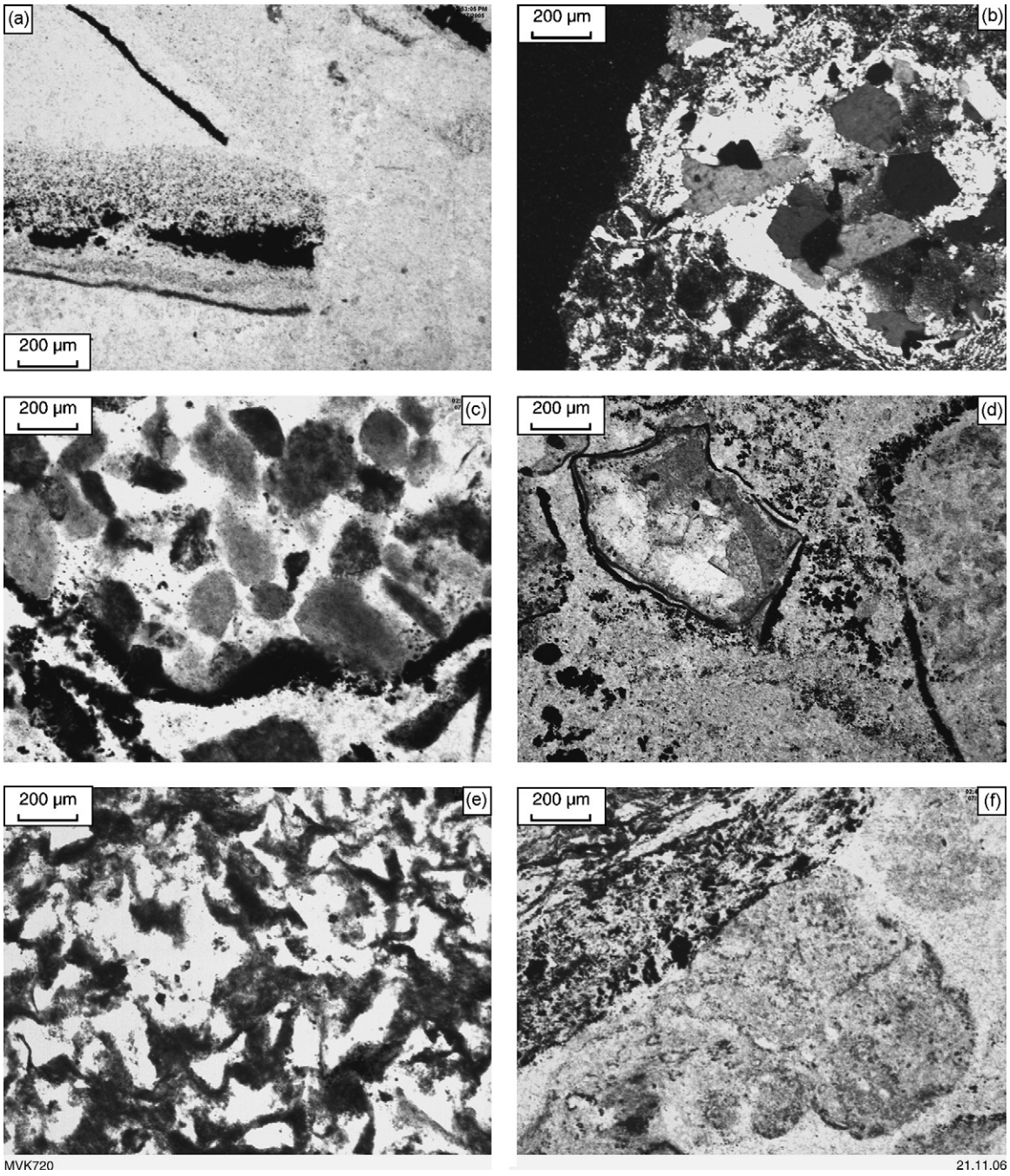

Fig. 12. (a) Plane polarised light thin section view from the lower part of member 3, showing clasts of pyrite-replaced carbonate; (b) cross-polarised light thin section view of plagioclase (albite) porphyritic volcanic clast from the lower part of member 3; (c) plane polarised light thin section view from the upper part of member 3, of a single clast of volcaniclastic sandstone in the upper 3/4 part of the image that is rimmed by pyrite: other smaller clasts that are largely replaced by pyrite occupy the lower part of the image; (d) plane polarised light thin section view from the upper part of member 3, of pyrite rims surrounding carbonate-altered volcanic (centre) and volcaniclastic rocks (right); (e) plane polarised light thin section view of a clast of welded tuff from member 3, composed of welded felsic glass shards in a matrix altered to chlorite and pyrite; (f) plane polarised light thin section view of the slump fault that separates the upper and lower parts of member 3, showing how it cuts volcanic clasts of the underlying lithology.

to 1 cm diameter, of texturally variable felsic volcanic rock (porphyritic, vesicular, etc.) and felsic volcaniclastic rock (Fig. 12c). The clasts have been thoroughly affected by chlorite–carbonate–pyrite alteration, including pyrite rims (Fig. 12d), and all feldspars have been recrystallized to microquartz and white mica. This bed grades up into felsic volcaniclastic sandstone and welded tuff that in turn passes up into ultra fine-grained felsic volcanic ash now represented by very fine-grained quartz and white mica. Welding is clearly indicated by the presence of fused cuspate felsic glass shards (Fig. 12e). Veins of microquartz and carbonate–microquartz–pyrite cut this unit at a high angle to bedding, and are unconformably overlain by rocks of member 5 (Figs. 10b and 11). The two subunits in this member are separated by a 1–3 mm thick seam of chlorite–pyrite–rutile (top of Fig. 10a) that contains a well-developed flow foliation and locally isoclinally folded clasts (Fig. 11). This seam cuts clasts in both the overlying and underlying volcaniclastic breccia beds (Fig. 12f) and lies at a moderate angle to bedding.

4.2.5. Member 5

The basal contact of member 5 is an unconformity on carbonate–microquartz–pyrite veins and host volcaniclastic rocks of underlying member 3. The unconformity surface is marked by a 1 mm thick bed with evenly spaced, small, euhedral tourmaline crystals and fine white mica flakes that are encrusted in pyrite (Figs. 10b, 11 and 13a). The unconformity surface is overlain by a thin layer (1–2 mm) of very finely bedded carbonate that is partly replaced by pyrite. The unconformity surface is overlain by a 1.5 cm thick bed of conglomerate composed of tabular silicified carbonate clasts in a matrix of replacive microquartz.

4.2.6. Member 6

Overlying member 5 is a 10 cm thick unit of finely laminated carbonates that are variably replaced by pyrite, grading up to black chert that is interpreted to represent silicified carbonates on the basis of more detailed observations described below (Figs. 10b and 11). The black chert contains finely dispersed clots

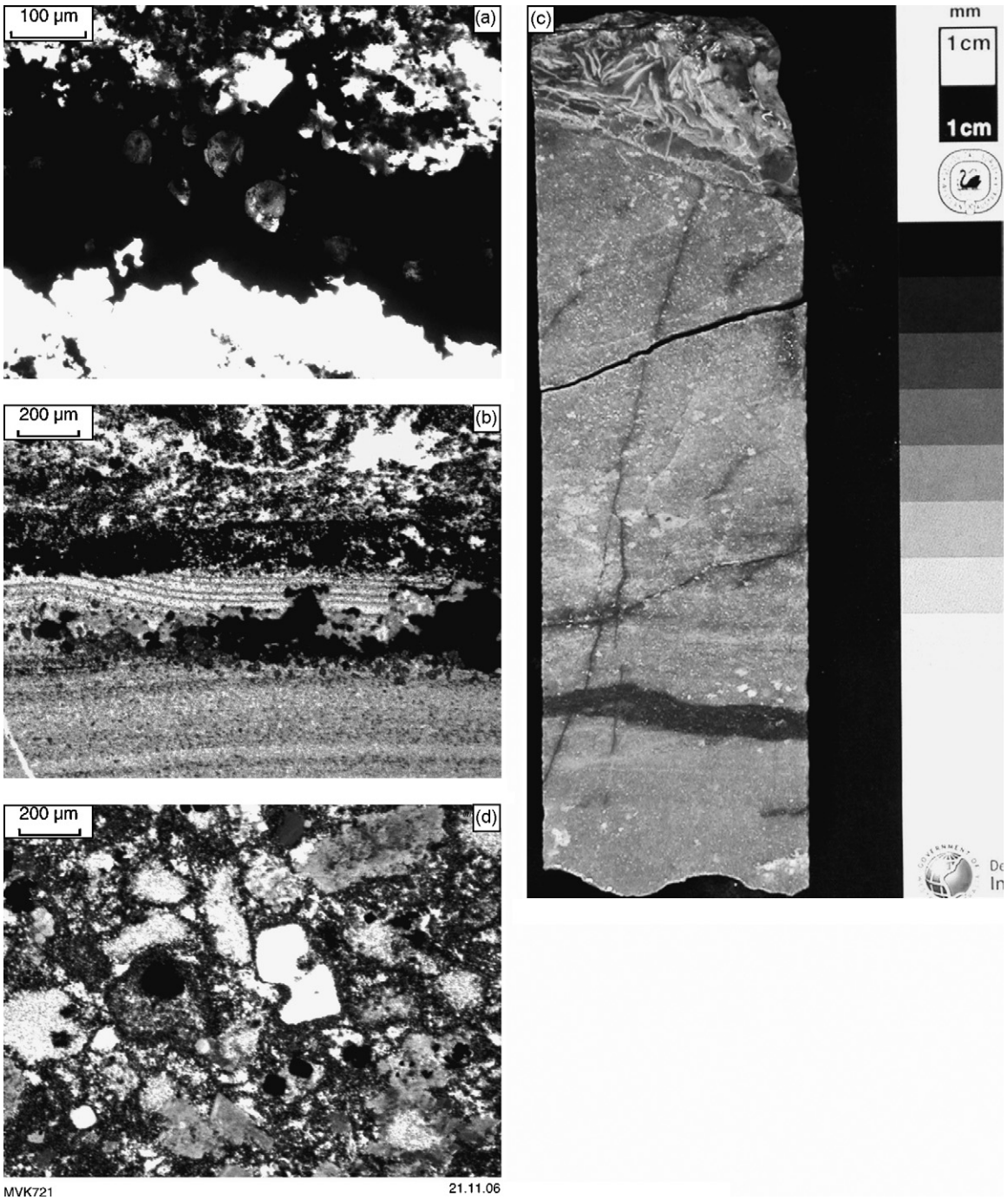

Fig. 13. (a) Plane polarised light thin section view of the unconformity at the base of member 5, showing small euhedral tourmaline crystals encrusted by pyrite (from 94.6 m in PDP2c); (b) plane polarised light thin section view of fine-scale bedding of carbonate rocks of member 6 that are extensively replaced by pyrite (from 94.5 m in PDP2c); (c) drillcore section of the volcanoclastic sandstone sampled for U–Pb zircon geochronology from 94.35 to 94.55 m in PDP2c; (d) cross-polarised thin section view of the silicified volcaniclastic sandstone shown in (c): note the rounded clasts of devitrified felsic volcanic glass (now microquartz and white mica), and the volcanic quartz crystal clast showing resorbed margins.

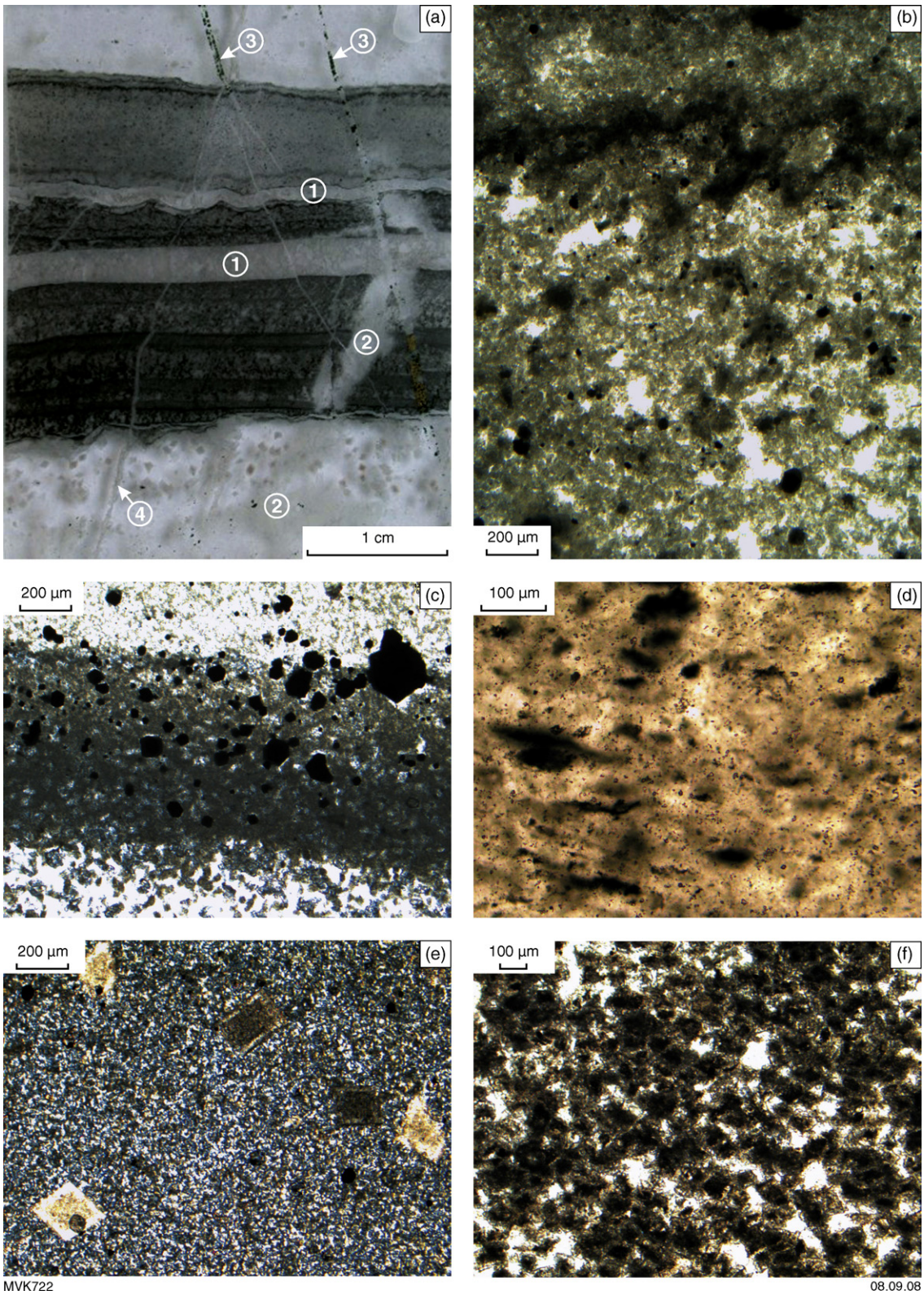

Fig. 14. Thin section features of bedded carbonate rocks of member 6: (a) whole thin section view of bedded micritic carbonate, showing fine-scale bedding defined by variations in texture and thin seams of dark matter along stylolitic bedding contacts. Note the four types of cross-cutting veins: (1) coarse carbonate veins parallel to bedding, (2) silica veins with euhedral carbonate rhombs that have jaspilitic cores, (3) quartz–chlorite–pyrite veins, (4) quartz veins (92.5 m in PDP2c); (b) plane polarised light thin section closeup of a), showing stylolitic bedding plane between carbonate beds with different textures; (c) plane polarised light thin section view of bedded carbonate quite thoroughly replaced by diagenetic pyrite (92.7 m in PDP2c); (d) plane polarised light thin section view of irregular clots of carbonaceous material in bedded carbonate (93.5 m in PDP2c); (e) cross-polarised light thin section view of silicified carbonate, with diagenetic dolomite rhombs and pyrite crystals (92.7 m in PDP2c); (f) plane polarised light thin section view of partly silicified carbonate, showing recrystallization texture of packed, zoned subhedral carbonate rhombs (sparry carbonate) that have dark cores and light rims.

and particles of carbonaceous material. Bedding is locally developed as very fine-scale couplets of light (carbonate) and dark (pyrite-rich) bands, with local small-scale, low-amplitude cross-beds that may represent either tidal (cf. Groves et al., 1981) or seasonal layering (Fig. 13b). Bedding in these rocks is inclined at 30° relative to bedding in both the underlying and overlying units, suggesting deposition on a local paleoslope (Figs. 10b and 11). Later replacement of the carbonate sediment by pyrite is clearly visible in thin sections (Fig. 13b).

A 15 cm thick bed of well sorted, fine-grained felsic volcaniclastic sandstone overlies the carbonates (Fig. 13c). This unit contains clasts of white mica-altered felsic volcanic material, less common clasts of devitrified felsic glass, numerous euhedral to subhedral volcanic quartz crystals (phenocrysts) with common resorbed margins, and volcanic quartz crystal shards (Fig. 13d). Two main beds are represented in this unit, each of them fining upwards to very fine-grained felsic ash. The top of the second bed is overlain by a 1.5–2 cm thick unit of flat pebble conglomerate (Fig. 13c) composed of curved tabular clasts (to 1.5 cm) of bedded felsic ash – now altered to silica and white mica – in a matrix of dark blue microquartz with rhombs of carbonate.

A 2 cm thick unit of thinly bedded carbonate that has been completely replaced by very fine-grained pyrite and intruded by white quartz veins overlies the felsic volcaniclastic unit. This passes up to 1.25 m (94.45–93.2 m) of faintly bedded carbonate (Fig. 6). These rocks are cut by bedding-parallel veins of microquartz with coarse carbonate rhombs, veins of coarse-grained carbonate, and veins of microquartz–pyrite–chlorite (Fig. 14a). The mineralogy of the bedded carbonate consists of carbonate, microquartz ± pyrite ± carbonaceous material ± haematite. Millimetre- to centimetre-scale bedding is well developed throughout the unit, defined by slight changes in texture, the amount of pyrite, and the amount of irregular clots of carbonaceous material (Fig. 14a–d). Graded bedding is common. Less common are very thin (<0.01 mm), wispy and slightly irregular, dark films of carbonaceous material along stylolites (Fig. 14b). These films overlie thin carbonate beds that contain finely dispersed carbonaceous material and pyrite, and display a distinctive secondary porosity texture now filled by sparry calcite. One of the carbonaceous stylolites is transected by a dewatering escape structure, in agreement with a diagenetic origin post-dating sedimentation.

Carbonate rocks from this part of the section show a variety of texture, including the micritic carbonates described above, micritic carbonate with sparsely distributed Fe-carbonate rhombs (to 1 mm large) and euhedral pyrite crystals (Fig. 14c and e). Microquartz varies in proportion across the unit, but locally accounts for up to 80% of the rock, where it has replaced the original carbonate and resulted in recrystallization to zoned Fe-carbonate rhombs with characteristic dusky cores and clear rims (Fig. 14f). In these layers, it is important to note that recrystallization did not affect the scattered pyrite crystals or the clots of carbonaceous material, which remain unaltered and in situ in the replaced matrix.

The bedded carbonate rocks of this member are cut by three layers of coarsely crystalline calcite breccia (Figs. 5, 6 and 15). Lowest in the section (at 94.1 m in PDP2c) is a 10–15 cm thick, white and green calcite breccia that is composed of coarse-grained white calcite with seams of chlorite that, in PDP2b, contains angular fragments of the fine-grained, grey, bedded carbonate hostrock. The calcite matrix has an angular, brecciated texture, with fragments lined by thin seams of chlorite and rutile: these minerals also fill spaces between carbonate crystals within the fragments. Contacts

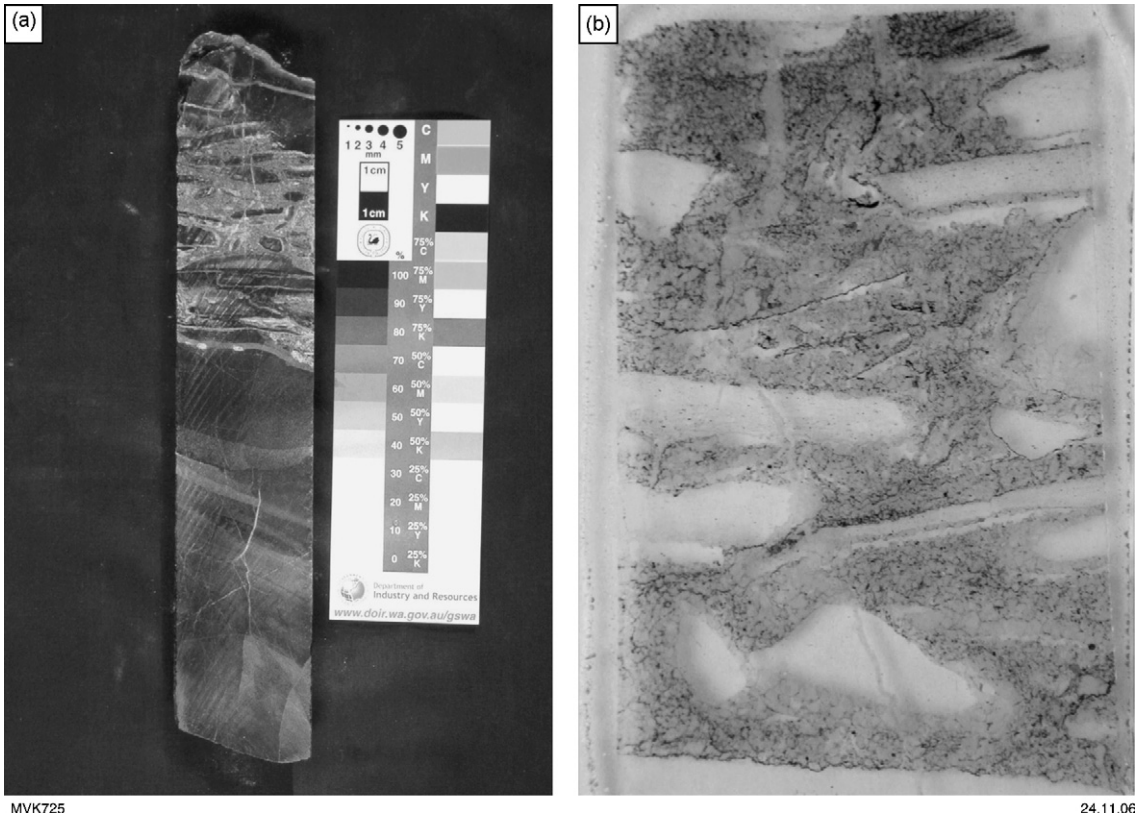

Fig. 15. (a) Section of drillcore PDP2c (93.2–93.5 m), showing bedded carbonate and discordant carbonate breccia of silicified carbonate clasts in matrix of coarsely recrystallized carbonate with chlorite–rutile–pyrite seams; (b) whole thin section view of carbonate breccia in (a), showing roughly aligned clasts of silicified carbonate and the coarsely crystalline nature of the matrix (width of view ~3 cm).

of the calcite with the bedded carbonate above and below vary from sharply planar to irregular.

Slightly higher (at 93.5 m depth in PDP2c) is a 1.5 cm thick layer of coarse-grained calcite that is separated from underlying and overlying, fine-grained, bedded carbonates by stylolites lined by chlorite and rutile. There are two stylolites at the base of this unit. The lowermost stylolite separates fine-grained, bedded carbonate below from 2 mm of coarsely crystalline calcite above. The main unit of coarsely crystalline calcite just above the second stylolite is 1 cm thick and contains a few, scattered, very small, angular clasts – more like flakes – of clear quartz and well-rounded carbonate, or carbonate-altered felsic volcanic, clasts. The coarse calcite spar in the matrix has well-developed drusy mosaic fabric, with crystals separated by an interstitial network of chlorite and rutile. This unit is capped by a third black, chloritic stylolitic contact with 2 mm of coarse crystalline calcite that contains several millimetre-size pyrite crystals but no chlorite.

Higher up again (at 93.3 m in PDP2c) is a 10–30 cm thick breccia of tabular, to rounded fragments of fine-grained, bedded, grey carbonate hostrock that has been completely silicified, in a matrix of coarsely crystalline calcite spar with thin rinds of chlorite and

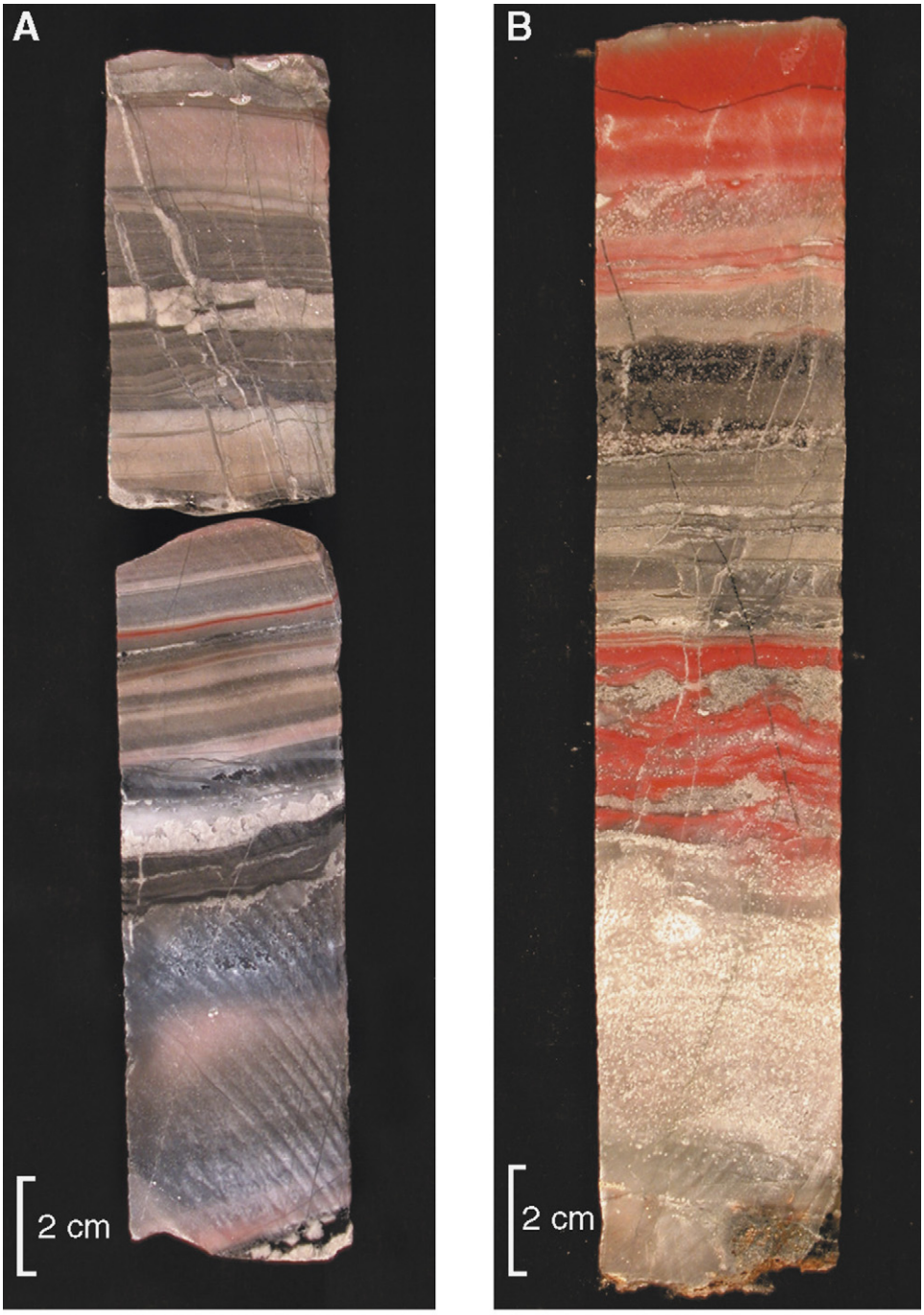

Fig. 16. (A) Section of drillcore PDP2c (92.7–93.2 m), showing haematite replacement of discrete carbonate beds, partial haematite replacement of others, and no haematite alteration in others; (B) section of drillcore at top of PDP2c (92.3–92.6 m), showing haematite replacement of discrete carbonate beds.

rutile (Fig. 15a). Discontinuous stylolites lined by chlorite occur in this unit, at all orientations (Fig. 15b).

Bedded carbonate rocks overlie the topmost breccia horizon and continue to the top of the sedimentary succession. These rocks are bedded at a fine to medium scale and contain faint, irregular traces of haematite colouration near the base, adjacent to a black chert vein (Fig. 16A). Haematite-altered carbonate becomes dominant in the uppermost 10–30 cm of the section, where it is interlayered with bedded carbonate (siderite + ankerite) and silica-replaced carbonate that are unaffected by haematite alteration (Fig. 16B).

In thin section, it was observed that much of the carbonate in member 6 has a weakly recrystallized texture of dark, zoned, subhedral carbonate rhombs in matrix of vaguely crystalline clear carbonate (Fig. 17a) with small pyrite crystals (labelled 'py' on Fig. 17a). An identical texture is preserved in haematite-altered carbonate higher up in the section, except that the core of dark carbonate rhombs are altered to haematite, giving the rocks their red colouration (Fig. 17b). Significantly, diagenetic pyrite in these haematite-altered carbonates has not been altered to haematite, even though the pyrite formed before, and independently of, the haematite alteration (Fig. 17b). In areas affected by more pervasive silica alteration near the jaspilitic top of the formation (Fig. 16b), the fine-grained carbonate precursor has been replaced by scattered, medium-size (1–2 mm) carbonate rhombs within a matrix of microquartz (Fig. 17c). Tiny crystals of haematite are present within the cores of the recrystallized carbonate rhombs, whereas the rims of these rhombs are clear (Fig. 17c).

4.2.7. Overlying pillow basalt

The upper part of the drillcore (69.3–92.3 m depth in PDP2c) is composed of pale green amygdaloidal pillow basalt with abundant interpillow hyaloclastite breccia. The mineral assemblage of this unit is a fine-grained mixture of Fe-rich chlorite–carbonate–pyrite ± rutile ± microquartz. Amygdales are filled by a rim of microquartz and a core of coarse-grained carbonate. The carbonate core of one amygdale was seen to contain haematite grains, as well as a minor amount of very fine-grained pyrite. No chert, carbonate, or barite veins cut this basalt unit, a feature also observed in outcrop.

4.3. Hyperspectral mapping of the drillcore

Multispectral logging of the core (see data in Van Kranendonk et al., 2006b) has identified hydrothermal kaolinite in the large white microquartz vein at the base of member 1, consistent with the observation of extensive hydrothermal kaolinite alteration footwall basalts and of hydrothermal kaolinite in hydrothermal chert veins in outcrop at the Dresser Mine and further along strike to the north (Van Kranendonk and Pirajno, 2004). Brown et al. (2006) discussed the difference between the spectra of hydrothermal kaolinite, which has a highly ordered crystallinity, and kaolinite formed by surficial weathering processes, which has a less well-ordered structure. Members with predominantly sedimentary rocks and hydrothermal silica + barite replacement show high bound water index values. Multispectral data from member 6 shows that the carbonate rocks are composed of an interlayered mixture of siderite, ankerite and calcite.

Multispectral data shows that the composition of chlorite changes about half way through the section of the overlying basalt unit (at ~77 m depth), from intermediate chlorite (in terms of Fe/Mg composition) at the top, to more Fe-rich chlorite in the lower half. Muscovite is common in the middle part of the unit, whereas epidote occurs towards the top of the hole, where secondary montmorillonite was also identified, representing the product of surficial

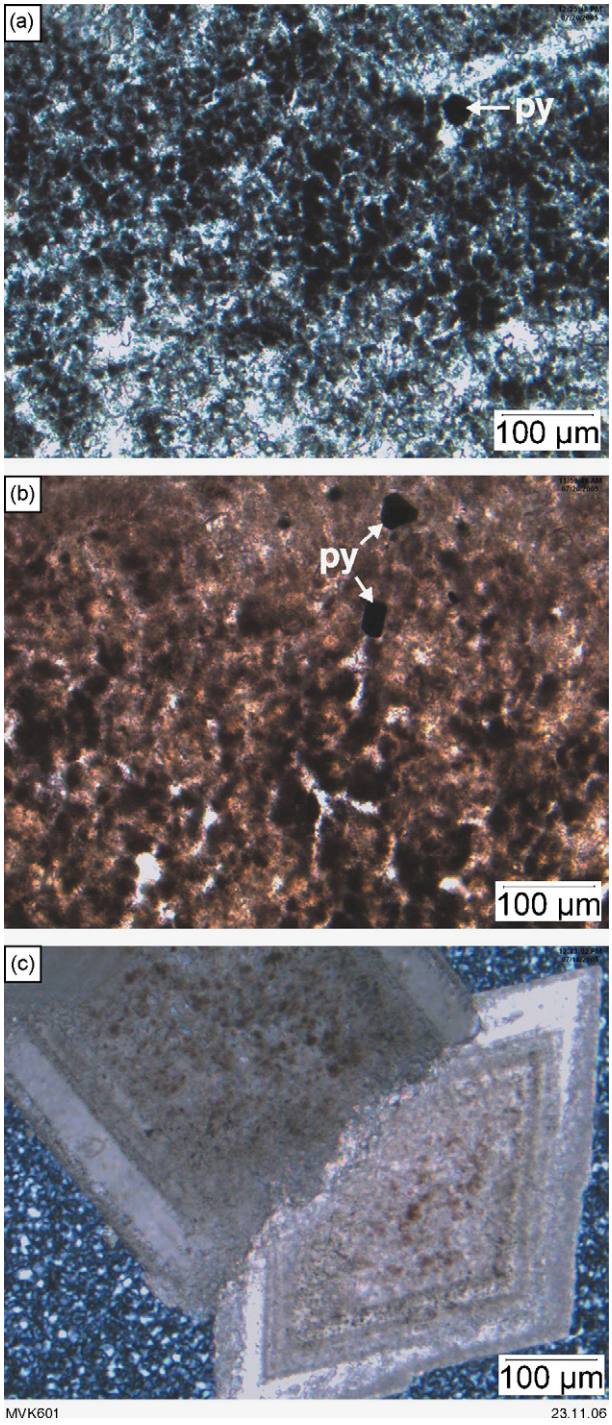

Fig. 17. Thin section views of haematite-altered carbonates: (a) plane polarised light thin section view of weakly haematite-altered carbonate, showing partly recrystallized texture of sparry carbonate with dark cores in which tiny haematite flakes occur, and pale rims. Note the diagenetic pyrite crystal (py) is unaltered, suggesting that haematite did not form as a result of oxidative processes (92.5 m in PDP2c); (b) plane polarised light thin section view of more heavily haematite-altered carbonate, showing a weakly recrystallized texture, similar to that in (a) and similar, unaltered diagenetic pyrite crystals (py) (92.7 m in PDP2c); (c) recrystallized, zoned carbonate rhombs in strongly silicified carbonate, showing cores with tiny haematite grains (92.5 m in PDP2c).

weathering. The carbonate composition in this unit is a mixture of siderite, calcite, and ankerite.

5. U–Pb geochronology

5.1. Method

Sample 180070 of approximately 100 zircons was extracted from about 120 g of volcaniclastic sandstone collected from member 6 of PDP 2c, using heavy liquid and magnetic separation techniques described by Nelson (1998). The zircons were collected from about half of the core shown in Fig. 13c. Grains were mounted in epoxy discs, polished to half their thickness, and photographed in transmitted and reflected light. Following the application of a high-purity gold coating, cathodoluminescence (CL) images of the zircons were acquired using a Philips XL30 scanning electron microscope housed by the Department of Applied Physics, Curtin University of Technology, in Perth, Western Australia.

Selected grains were analysed by sensitive high-resolution ion microprobe (SHRIMP-II) in the John de Laeter Centre of Excellence in Mass Spectrometry at Curtin University. SHRIMP U–Th–Pb analytical procedures followed those described by Compston et al. (1984) and Nelson (1998). Grains were sputtered using an O_2^- primary beam, and six cycles of sequential measurements of the $^{90}Zr_2O^+$, $^{204}Pb^+$, background (204.1), $^{206}Pb^+$, $^{207}Pb^+$, $^{208}Pb^+$, $^{238}U^+$, $^{232}ThO^+$and $^{238}UO^+$peaks in the secondary ion beam were made, using an electron multiplier in pulse counting mode. Fractionation in the measured Pb/U ratio was monitored by reference to the CZ3 zircon standard ($^{206}Pb/^{238}U = 0.0914$, age = 564 Ma). Common-Pb corrections were carried out using measured ^{204}Pb (Compston et al., 1984), and common-Pb isotopic compositions determined

Table 2
U–Pb SHRIMP analytical results for zircons from sample GSWA 180070

Sequence number[a]	Grain spot	U (ppm)	Th (ppm)	Th/U	$f204$[b] (%)	$^{208}Pb/^{232}Th$	±1σ	$^{238}U/^{206}Pb$	±1σ	$^{207}Pb/^{206}Pb$	±1σ	$^{207}Pb/^{206}Pb$ age (Ma)	±1σ	D[c] (%)
Youngest zircon (2 analyses of 1 grain, arranged by ascending $^{207}Pb/^{206}Pb$ age)														
6	6.1	542	191	0.36	0.248	0.1838	0.0020	1.394	0.009	0.30188	0.00053	3479.9	2.7	−0.2
21	6.2	492	199	0.42	0.161	0.1827	0.0036	1.409	0.027	0.30224	0.00046	3481.7	2.3	0.7
Older zircons (31 analyses of 31 grains, arranged by ascending $^{207}Pb/^{206}Pb$ age)														
26	25.1	318	204	0.66	0.360	0.1844	0.0036	1.424	0.026	0.30705	0.00089	3506.2	4.5	2.2
16	16.1	133	61	0.47	0.228	0.1777	0.0023	1.435	0.011	0.30895	0.00126	3515.7	6.3	3.1
17	17.1	76	40	0.55	0.114	0.1809	0.0026	1.395	0.013	0.30929	0.00126	3517.4	6.3	1.0
12	12.1	269	132	0.51	0.308	0.1904	0.0027	1.412	0.009	0.30954	0.00085	3518.6	4.2	1.9
40	39.1	192	107	0.58	0.519	0.1787	0.0062	1.393	0.026	0.30956	0.00239	3518.7	11.9	0.8
5	5.1	468	155	0.34	0.041	0.1846	0.0019	1.383	0.011	0.30988	0.00052	3520.3	2.6	0.3
43	42.1	246	92	0.39	0.543	0.1807	0.0066	1.416	0.026	0.30994	0.00092	3520.6	4.6	2.2
29	28.1	114	47	0.43	0.032	0.1868	0.0040	1.413	0.027	0.31002	0.00121	3521.0	6.0	2.0
32	31.1	165	67	0.42	0.914	0.1834	0.0049	1.404	0.026	0.31007	0.00124	3521.2	6.2	1.6
34	33.1	356	192	0.56	0.618	0.1622	0.0090	1.460	0.033	0.31008	0.00265	3521.3	13.2	4.5
41	40.1	157	72	0.48	0.071	0.1783	0.0036	1.440	0.027	0.31019	0.00092	3521.8	4.6	3.5
25	24.1	181	100	0.57	0.139	0.1867	0.0037	1.393	0.026	0.31022	0.00086	3522.0	4.3	1.0
7	7.1	324	114	0.36	0.048	0.1882	0.0017	1.376	0.009	0.31029	0.00062	3522.4	3.1	0.0
24	23.1	223	117	0.54	0.266	0.1883	0.0043	1.420	0.030	0.31034	0.00084	3522.6	4.2	2.4
10	10.1	185	100	0.56	0.084	0.1864	0.0019	1.370	0.011	0.31046	0.00080	3523.2	4.0	−0.3
38	37.1	151	60	0.41	0.044	0.1856	0.0046	1.411	0.026	0.31050	0.00117	3523.4	5.8	2.0
36	35.1	322	109	0.35	0.558	0.1855	0.0047	1.414	0.025	0.31070	0.00081	3524.4	4.0	2.2
14	14.1	297	225	0.78	0.017	0.1893	0.0015	1.377	0.008	0.31076	0.00063	3524.7	3.1	0.2
11	11.1	355	167	0.49	0.014	0.1875	0.0026	1.389	0.008	0.31094	0.00060	3525.6	3.0	0.8
18	18.1	130	58	0.46	0.083	0.1855	0.0022	1.381	0.010	0.31094	0.00096	3525.6	4.8	0.4
19	19.1	63	28	0.46	0.324	0.1734	0.0040	1.413	0.022	0.31159	0.00148	3528.8	7.3	2.2
9	9.1	243	140	0.60	0.436	0.1882	0.0024	1.388	0.009	0.31164	0.00087	3529.1	4.3	0.9
33	32.1	347	138	0.41	0.751	0.1845	0.0098	1.418	0.025	0.31167	0.00134	3529.2	6.6	2.5
3	3.1	220	130	0.61	0.355	0.1875	0.0024	1.397	0.009	0.31176	0.00098	3529.7	4.8	1.4
20	20.1	417	121	0.30	0.307	0.1819	0.0022	1.409	0.009	0.31193	0.00062	3530.5	3.1	2.1
22	21.1	122	54	0.45	−0.017	0.1981	0.0049	1.332	0.026	0.31198	0.00098	3530.8	4.9	−2.3
2	2.1	197	78	0.41	0.264	0.1799	0.0030	1.420	0.011	0.31200	0.00108	3530.8	5.3	2.7
1	1.1	161	61	0.39	0.059	0.1894	0.0024	1.384	0.013	0.31237	0.00094	3532.7	4.7	0.8
39	38.1	139	67	0.50	0.009	0.1854	0.0037	1.402	0.026	0.31239	0.00099	3532.8	4.9	1.8
30	29.1	279	113	0.42	0.217	0.1832	0.0037	1.394	0.025	0.31258	0.00076	3533.7	3.7	1.3
8	8.1	183	106	0.60	0.765	0.1887	0.0025	1.405	0.009	0.31281	0.00111	3534.9	5.5	1.9
Analyses with $f204 > 1\%$ and/or $D > 5\%$ (10 analyses of 10 grains, arranged by ascending D)														
31	30.1	182	133	0.75	1.184	0.1925	0.0043	1.409	0.026	0.31222	0.00137	3531.9	6.8	2.1
13	13.1	167	80	0.50	1.108	0.1772	0.0044	1.443	0.010	0.30998	0.00151	3520.8	7.5	3.6
23	22.1	357	188	0.54	0.195	0.1741	0.0031	1.487	0.027	0.30432	0.00065	3492.3	3.3	5.1
15	15.1	110	42	0.40	0.307	0.1702	0.0030	1.482	0.012	0.31103	0.00118	3526.0	5.8	5.7
27	26.1	327	131	0.41	0.580	0.1753	0.0037	1.490	0.027	0.31032	0.00081	3522.5	4.0	6.0
35	34.1	206	171	0.86	1.469	0.1664	0.0062	1.537	0.028	0.30132	0.00259	3477.0	13.3	7.1
28	27.1	219	150	0.71	1.240	0.1643	0.0039	1.534	0.028	0.30923	0.00135	3517.1	6.7	8.0
37	36.1	299	264	0.91	1.157	0.1612	0.0043	1.587	0.036	0.30167	0.00142	3478.8	7.3	9.4
42	41.1	194	142	0.76	1.267	0.1601	0.0053	1.622	0.029	0.29909	0.00148	3465.5	7.7	10.7
4	4.1	213	84	0.41	0.108	0.1887	0.0019	1.591	0.010	0.31047	0.00084	3523.3	4.2	10.8

All of the tabulated ratios are corrected for common-Pb.

[a] Numbered in order of acquisition (1–20 on 15 December 2005, 21–43 on 3 August 2006).

[b] $f204 = 100 \times (\text{common } ^{206}Pb)/(\text{total } ^{206}Pb)$.

[c] $D = 100 \times (^{207}Pb/^{206}Pb \text{ age} - ^{238}U/^{206}Pb \text{ age})/(^{207}Pb/^{206}Pb \text{ age})$.

using the method of Stacey and Kramers (1975) were assumed. The decay constants used were those recommended by Steiger and Jäger (1977), and the data were processed using SQUID v1.10 and Isoplot v3.06 (Ludwig, 2001, 2003), with discordance (D) recalculated as

$$D = 100 \times \frac{^{207}\text{Pb}/^{206}\text{Pb age} - ^{206}\text{Pb}/^{238}\text{U age}}{^{207}\text{Pb}/^{206}\text{Pb age}}$$

All ages quoted are ^{204}Pb-corrected ^{207}Pb/^{206}Pb dates unless specified otherwise.

The data (Table 2) were acquired in two separate analytical sessions. The first (on 15 December 2005) utilised a primary beam with a 30 μm diameter spot, and encompassed analyses 1.1–20.1 inclusive, together with 13 interspersed measurements of the CZ3 standard. The second (on 3 August 2006) used a 20 μm diameter spot (in order to target smaller grains), and encompassed analyses 6.2 and 21.1–42.1 inclusive, together with nine interspersed measurements of the CZ3 standard. The measurements of the standard defined 1σ uncertainties of 0.18% (first session) and 0.65% (second session) associated with the internal error of the weighted mean ^{238}U/^{206}Pb ratio of CZ3, and 0.41% (first session) and 1.65% (second session) associated with its spot-to-spot reproducibility. The precision of each tabulated ^{238}U/^{206}Pb ratio includes both of the relevant (session-specific) uncertainties, summed in quadrature.

Where possible, the ion probe spot was sited within crystal terminations in order to minimise the chance of encountering xenocrystic cores, as inherited material within grains is of limited interest in the determination of maximum depositional ages.

5.2. Results

The zircons collected from sample 180070 are pale- to dark brown and translucent to opaque in transmitted light, and range in size from 35 μm × 50 μm to 80 μm × 150 μm. Prominent concentric oscillatory zoning is a common feature of their CL emission, and some grains preserve well-developed pyramidal terminations (Fig. 18), but most are subhedral and partly rounded, consistent with mechanical abrasion during sedimentary transport.

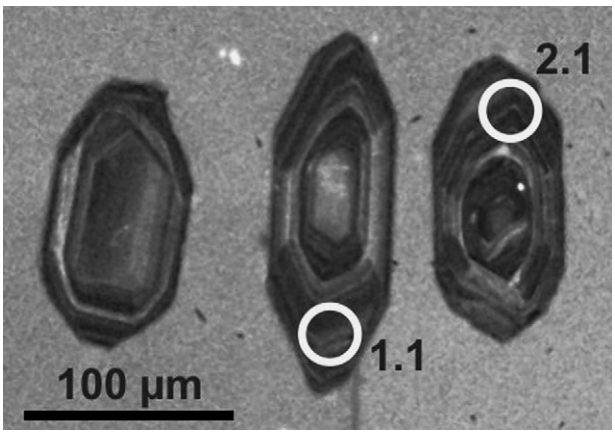

Fig. 18. Cathodoluminescence (CL) image of representative zircons separated from sample 180070, showing igneous growth zoning and euhedral prismatic shapes. Numbered circles approximate the diameter and position of SHRIMP spots, and are labelled with grain and spot (see Table 1).

A total of 43 analyses were obtained from 42 zircons (Table 2, Figs. 19 and 20). Ten analyses of 10 zircons were characterised by relatively high common-Pb contents (f204 > 1%) and/or moderate to strong discordance (D > 5%). These results are generally either imprecise or unreliable, and are not considered further. The remaining 33 analyses of 32 zircons fell into two categories:

(1) Two analyses (6.1 and 6.2) of grain 6, which yielded a weighted mean age of 3481.0 ± 3.6 Ma (2σ), and;
(2) 31 analyses of 31 zircons, with ages spanning the interval 3540–3500 Ma. Excluding analysis 25.1, which yielded a slightly younger age, the other 30 analyses define a single population (MSWD = 1.2) with a weighted mean age of 3525.3 ± 1.8 Ma (95% confidence).

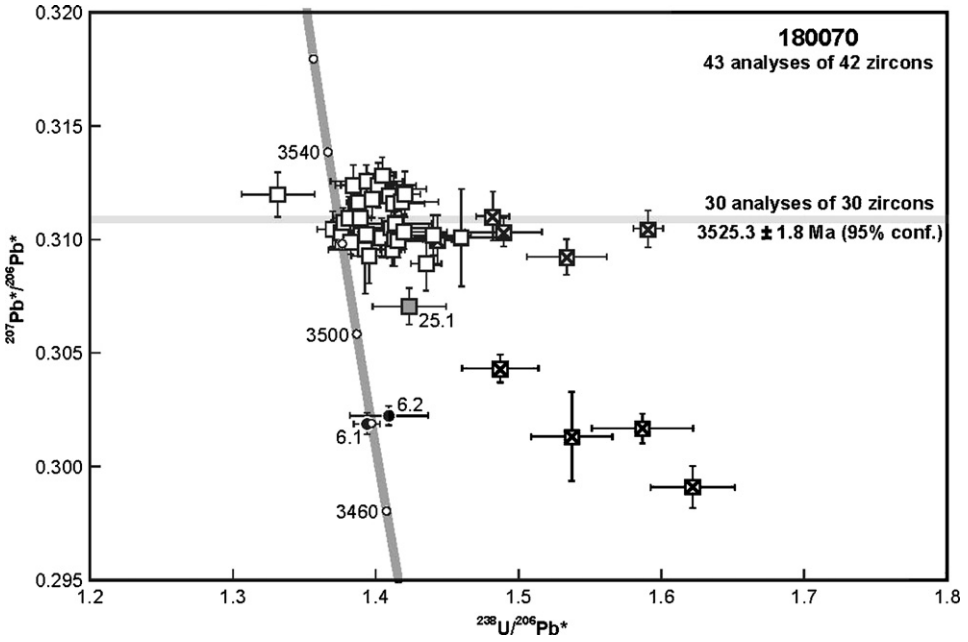

Fig. 19. U–Pb analytical data for zircons from sample 180070. Black circles (6.1 and 6.2) denote analyses of the youngest detrital zircon, open squares denote analyses within the main older population, the grey square (analysis 25.1) is a younger outlier from this population, crossed open squares denote ungrouped analyses (f204 > 1% or D > 5%). Error-bars are 1σ.

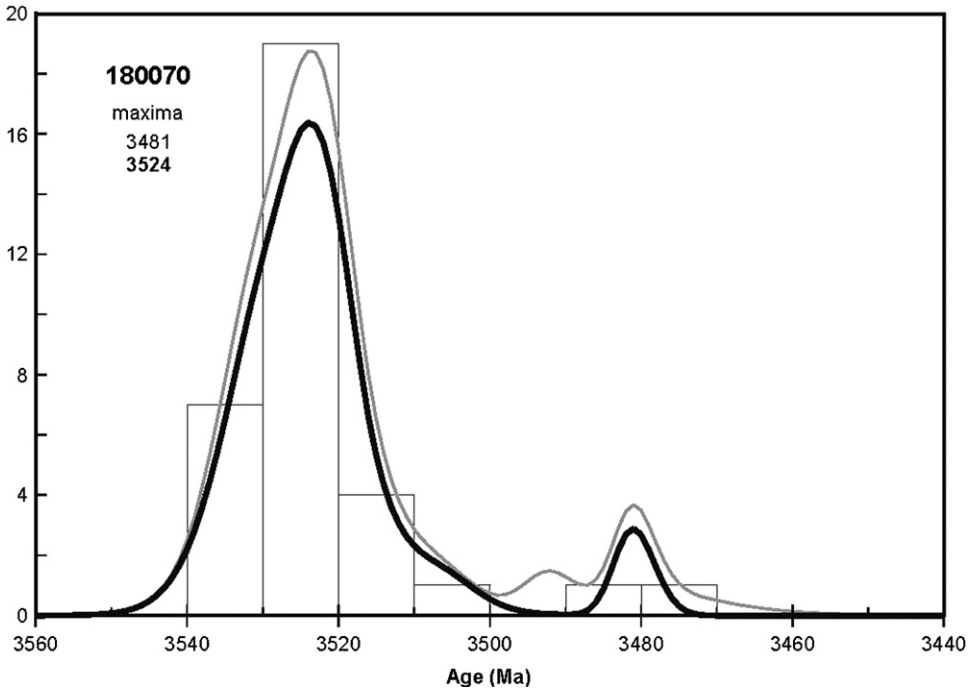

Fig. 20. Probability density diagram for analysed zircons from sample 180070. Black curve, maxima values, and frequency histogram (bin width 10 Ma) include only data with $f204 < 1\%$ and $D < 5\%$ (33 analyses of 32 zircons). Grey curve includes all data (43 analyses of 42 zircons).

5.3. Interpretation

There are two possible interpretations of these data. It is conceivable that the dominant ca. 3525 Ma age reflects igneous crystallization of a dominant magmatic component in this volcaniclastic rock, and provides an approximation of its depositional age. In this scenario, grain 6 (which has the highest U content of all of the analysed grains) was affected by near-complete loss of radiogenic Pb at ca. 3480 Ma, but did not experience any more recent Pb-loss events of the type responsible for discordance in several of the other analyses. Alternatively, the ca. 3525 Ma age may simply reflect the dominant zircon-bearing provenance of this volcano-sedimentary rock, with grain 6 representing a minor detrital age component and thus a maximum age for deposition of the rock of ca. 3481 Ma.

The second of these interpretations is considered the more likely, for two reasons. Firstly, the anomalously young age initially derived from grain 6 was faithfully reproduced during the second analytical session. Secondly, linking this young age to ancient radiogenic-Pb loss (as a consequence of radiation damage to the zircon lattice) is problematic, because the U content of grain 6 is only marginally higher than that of the other grains. Furthermore, grain 6 displays no evidence for recent loss of Pb, in contrast to several of the lower-U, discordant grains ($D > 5\%$) that underwent *only* recent Pb-loss.

Consequently, we consider the age of 3481.0 ± 3.6 Ma (2σ) to constitute a maximum age for the deposition of the volcaniclastic unit represented by sample 180070, and we attribute the ca. 3525 Ma zircon age population to the dominant zircon-bearing rock or suite within the sedimentary source region. In practical terms, the fact that the zircon profile preserves no record of the East Pilbara-wide episode of voluminous, 3470–3460 Ma felsic volcano-plutonic activity (exemplified by the erupted Duffer Formation and the granitic Callina Supersuite; Van Kranendonk et al., 2007) means that the actual depositional age was very probably restricted to the interval between the youngest detrital zircon age (3481 Ma) and prior to 3470 Ma.

6. Discussion

6.1. Regional correlations of stratigraphy

A significant result from inspection of the diamond drill core through the Dresser Formation is the recognition that surface outcrops of layered chert represent the altered equivalents of bedded carbonate rocks at depth, highlighting the effects of surficial silicification during late Eocene to Oligocene Australian weathering (van de Graaff, 1983). However, this does not mean that *all* silicification was late, as veins of chert are ubiquitous in, and restricted to, the footwall, and are unconformably overlain by non-silicified volcanic rocks (cf. Van Kranendonk, 2006). Black- and red-weathering surface outcrops of wrinkly stromatolitic laminates are the surface-altered equivalents of laminated pyrite at depth in fresh drillcore: textural evidence shows that the pyrite is, at least locally, replacive of sedimentary carbonate.

In order to place the drillsite stratigraphy in a more regional context, three other sections were measured through the lower chert–barite unit of the Dresser Formation along strike and compared with sections measured by previous workers (Fig. 21). The six members identified at the drillsite can be identified in the other sections, although correlation is speculative in some. A significant observation is the recognition of members 1 and 2 between sections in the north and south, consisting of a basal member of carbonate with minor sandstone that grades up into bedded carbonate with small, radiating crystal splays (?gypsum), to rippled carbonate, to wrinkly laminated stromatolite. Apart from this, however, the regional comparison highlights the significant lateral stratigraphic variations first noted by Groves et al. (1981) and interpreted by Nijman et al. (1998) as due to growth faulting.

The regional stratigraphic comparisons provided here confirm that the Dresser Formation was deposited during tectonic instability that was most likely due to growth faulting. This is particularly evident from comparison of section C with adjacent sections. In section C, the distinctive horizon of wrinkly laminated stromatolitic

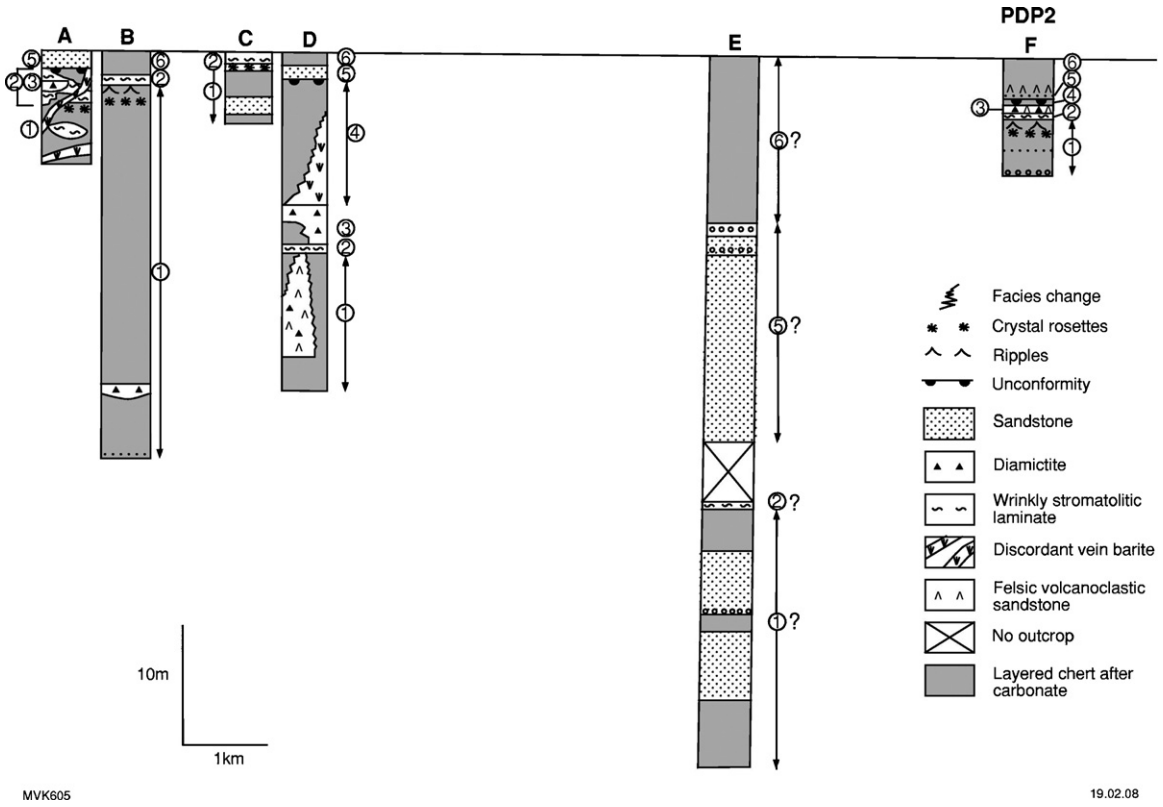

Fig. 21. Stratigraphic sections through the Dresser Formation, from north to south across the North Pole Dome. Section locations are shown in Fig. 2. Sections B and E from Nijman et al. (1998), but assignation of members the results of this study; section F is a composite of the data from drillsite PDP2.

rocks of member 2 are directly overlain by pillow basalt, indicating that members 3–6 are missing in this area. This contrasts sharply with section D, only 700 m to the south, which contains these upper members. The most likely interpretation is that this rapid lateral facies variation is because of non-deposition of members 3–6 in this area and that it represents a structural high during deposition, bounded by growth faults that became active after deposition of member 2. However, significant thickness variations in members 1, 3, 4, 5 and 6 along strike suggest active growth faulting throughout deposition of these members, as well. A maximum stratigraphic thickness of sediment at section E, combined with a far greater thickness of clastic sediment in this section, suggests maximum basin subsidence in this area. As discussed below, this section is from the heart of the hydrothermal system, where barite was mined from massive veins in the footwall (see Section 6.4).

Direct evidence of growth faulting is present in the form of drag folds along the contact between downfaulted silicified carbonate sediments of the lower Dresser Formation chert and footwall metabasalts at the locality of section D (Fig. 22). The coarse, unsorted conglomerate horizons also provide good evidence of active, syn-depositional growth faulting (see also Nijman et al., 1998).

Section A, at the far northern limit of the Dresser Formation, contains a relatively thin sedimentary succession that pinches out to the west, has the thickest section of wrinkly laminated stromatolite with the largest stromatolites (see Fig. 12 in Van Kranendonk, 2006), and is the only site with observed desiccation cracks. These observations suggest that Section A was the shallow water margin of the basin.

In section D, a coarse breccia with barite blocks up to 10 m long (see Fig. 13 in Van Kranendonk, 2006) was found to have a fine-grained matrix of felsic volcaniclastic material, including glass shards that have textures indicative of formation as a hyaloclastite (Fig. 23a). The rock has been silicified, but the shards can be inferred as originally felsic in composition on the basis that no traces of opaques are present, as would be expected from a mafic protolith.

In section C, the top of member 1 is characterised by a distinctive unit of centimetre-layered carbonate–chert rock, consisting of dark brown carbonate layers, which have an internal texture of interlocking rhombic Fe-carbonate crystals, and layers of pale grey-green chert. Chert layers have gradational lower contacts with carbonate layers, but commonly sharp upper contacts with overlying carbonate layers. The chert layers are distinct in colour and texture from hydrothermal vein chert and commonly contain the remnants of crystal rosettes, interpreted previously as gypsum (Fig. 23b: Groves et al., 1981; Buick and Dunlop, 1990).

6.2. Mineral paragenesis during sedimentation, diagenesis, and hydrothermal fluid circulation

Evidence gathered from the inspection of drillcore intersections indicates alternations between marine precipitation of carbonates and pulses of at least two types of hydrothermal fluids that, together, precipitated a common sequence of minerals.

From thin section studies of mineral paragenesis, it was found that sedimentary carbonate was the earliest mineral precipitate at several different levels in the stratigraphy (e.g., Fig. 9a). Trace element analysis of carbonate from the lower part of the Dresser Formation (member 1 from regional section C) indicates Fe-rich carbonate precipitation from seawater (Garcia-Ruiz et al., 2003; Van Kranendonk et al., 2003). Foriel et al. (2004) was able to identify this seawater component in fluid inclusions from quartz in lava escape

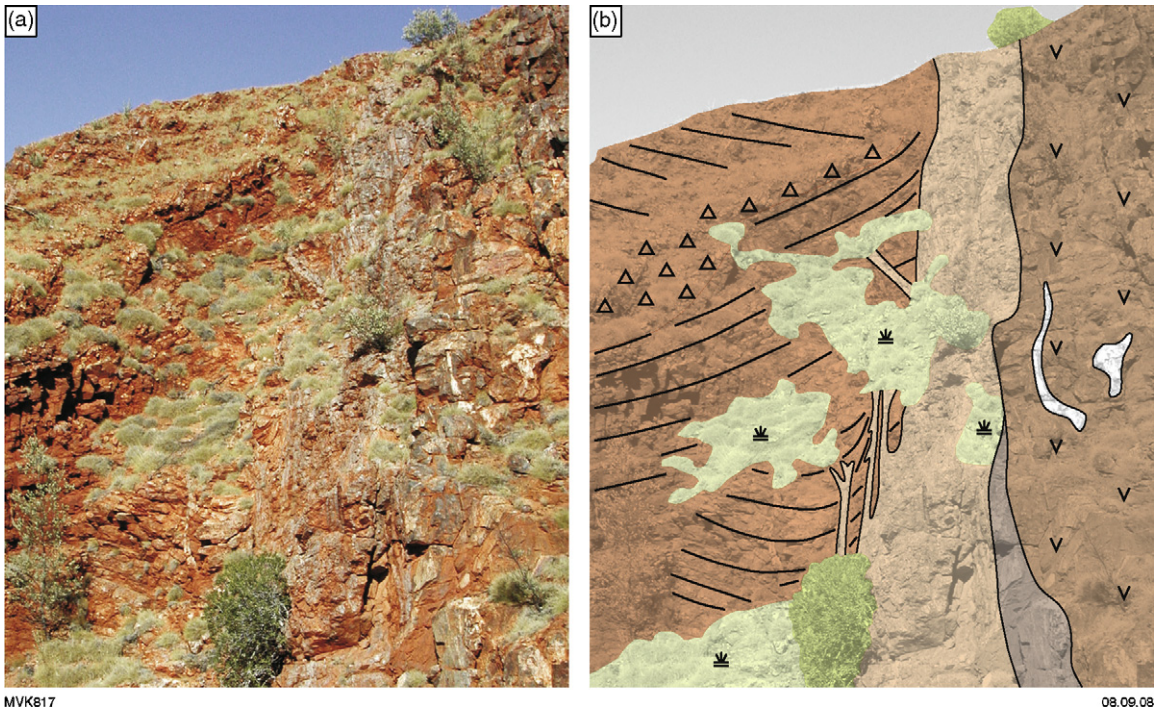

Fig. 22. (a) Outcrop photograph and (b) interpreted line drawing of the basal Dresser Formation chert–barite unit in fault contact with footwall volcanics (v-pattern on right side of part b) at the locality of section D of Fig. 22 (see Fig. 2 for locality). Smooth lines indicate bedding traces in chert–barite unit; pale brown = coarse barite vein; white = quartz vein; grey = chert vein; triangles = diamictite unit; cover indicated by bush pattern. Note the drag fold of bedding in the lower part of the chert–barite unit against the massive barite vein, which is interpreted to occupy a growth fault. Note also how the diamictite unit cuts down across bedding in underlying rocks and the onlap of overlying bedded chert (silicified carbonate), indicating large-scale tilting of bedding during sediment accumulation. Cliff is ~20 m high.

tubes of overlying pillow basalts, and showed that it was similar to modern seawater, except for a higher concentration of dissolved salts.

Textural evidence suggests that sedimentary carbonate was affected by three styles of diagenetic alteration. Layered carbonate rocks of member 1, which lie just beneath rippled carbonate sandstones and wrinkly laminated stratiform stromatolites with local desiccation cracks, have been affected by the growth of diagenetic gypsum(?) crystal rosettes and silicification (Fig. 23b: Buick and Dunlop, 1990). That the gypsum(?) crystal rosettes occur at the only level in the stratigraphy where there is evidence of shallow water and locally exposed conditions, suggests crystal growth due to evaporation, as originally proposed, in a locally sulfate-enriched basin (Groves et al., 1981; Buick and Dunlop, 1990; Van Kranendonk, 2006). The other styles of diagenetic alteration occur in member 6, where micritic carbonate rocks were affected by the crystallization of scattered pyrite crystals, and dolomitization, both of which may well have resulted from microbial activity (cf. Fig. 14c and e: e.g., Berner, 1970; Vasconcelos and McKenzie, 1997).

In member 1, sediment accumulation of seawater carbonate was followed by widespread, repeated pulses of hydrothermal fluid circulation that resulted in further, much more complete alteration of carbonates. Early pulses resulted in precipitation of large volumes of pyrite, principally as a replacement of bedded carbonates (e.g., Figs. 7c, 8b and 13b), but also (possibly) as primary precipitates on the seafloor (e.g., Fig. 7a). Sulfur isotope studies indicate $\delta^{34}S$ values of −0.9‰ for laminated pyrites, indicating a mantle source for the sulfur (Lambert et al., 1978; Philippot et al., 2007). Map and petrographic data presented herein and elsewhere indicate that the pyrite was introduced by a hydrothermal source (e.g., Foriel et al., 2004; Van Kranendonk, 2006).

Episodes of pyrite replacement were followed by crystallization of barite + silica ± sphalerite (with local secondary pyrite and carbonate) from later fluids. This happened repeatedly in the accumulation of member 1, as indicated by sandstone with pyrite-rimmed barite clasts in the middle part of member 1 that is overlain by further thicknesses of laminated barite–pyrite (Fig. 9a and b). This observation is important because it shows that (1) there were repeated episodes of barite-rich fluids entering, crystallizing, and being eroded in the system during sediment accumulation, and (2) periods of barite crystallization (and locally, erosion) alternated with periods of pyrite replacement during sediment accumulation. The textural observations pertaining to barite crystallization in the chert–barite unit described herein, when combined with observations of barite in massive silica + barite veins in the footwall (Van Kranendonk, 2006), show that the barite present in the bedded sedimentary rocks represents a replacement of pyrite-altered sedimentary carbonate as a result of hydrothermal fluid circulation (Figs. 7b and c and 9a). Careful observation shows that barite in veins parallel to primary bedding crystallized from horizontal crack-seal veins (e.g., Figs. 7c and 9a: cf. Hodgson, 1989). Some barite replacement occurred at a very early stage, as evidenced by barite crystals that have pushed up wet sediment in some localities (see Fig. 11d in Van Kranendonk, 2006) and by eroded barite crystal tops beneath sandstone beds in some other localities (e.g., Fig. 9a). Although gypsum(?) crystal rosettes are developed at one stratigraphic level (e.g., Figs. 21 and 23b), these are independent from the barite crystals that, despite claims by previous authors that interfacial angles of barite crystals indicate a gypsum precursor (Lambert et al., 1978; Buick and Dunlop, 1990), more recent studies have shown a primary origin of barite crystals (Runnegar et al., 2001).

Textural data presented herein, together with previous sulfur isotope studies from the Dresser Formation (Lambert et al., 1978) and other deposits (e.g., Rye, 1993), indicate that barite was not precipitated in equilibrium with the pyrite that is present in pyritic

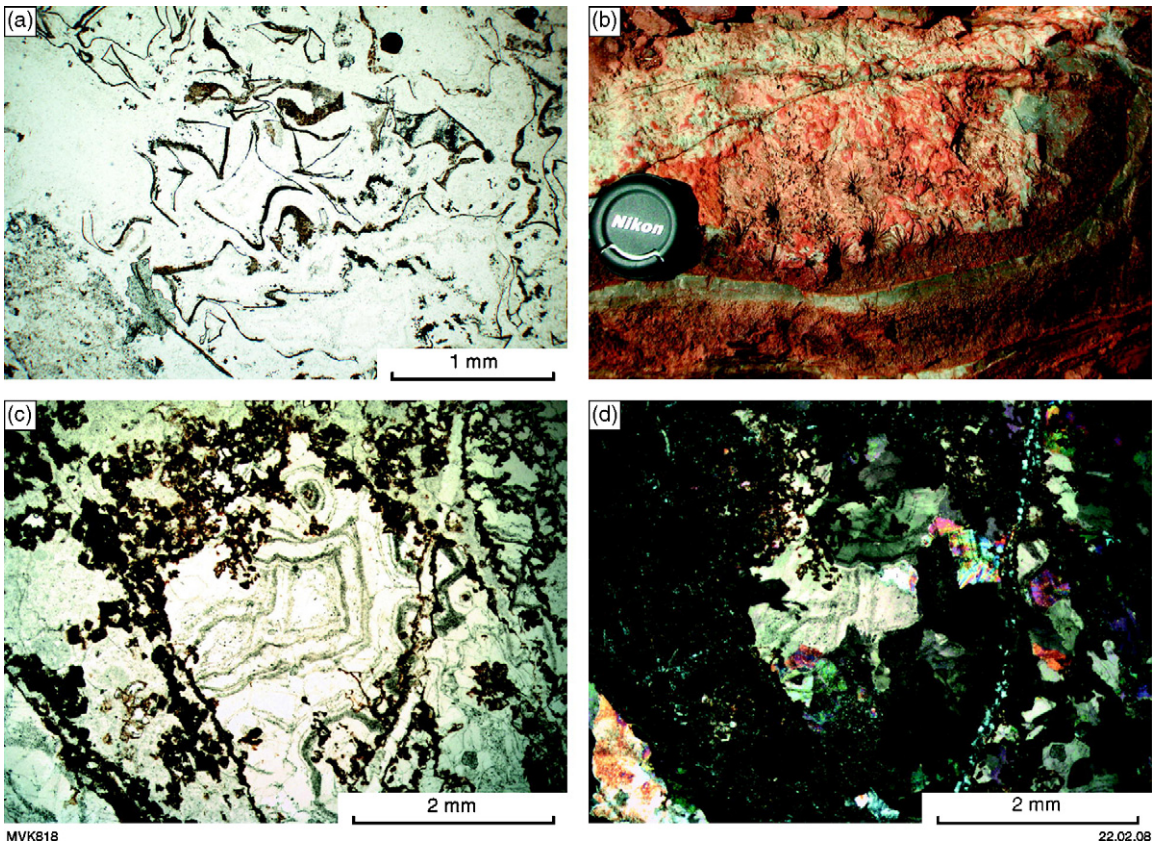

Fig. 23. (a) Plane polarised light thin section view of felsic hyaloclastite from the base of the Dresser Formation at section D. (b) Outcrop view of spherical radiating crystal splays of what were possibly formerly gypsum, in layered ankerite-chert rock from the top of member 1 in section C; (c and d) plane polarised and cross-polarised light thin section views, respectively, of radiating crystal splays of what were probably formerly gypsum from Fig. 19b. Former crystal outlines are from bottom right to top left of view, and are outlined by a rind of dark carbonate. Large crystal in centre is filled by coarsely crystalline hydrothermal aragonite with distinct colloform banding, indicating a late replacement origin of the aragonite. Microquartz fills the areas between the aragonite-filled crystals.

laminates, but was introduced by (a) later hydrothermal fluid(s) with a distinct composition. Foriel et al. (2004) identified this fluid as also of hydrothermal origin, but lower temperature (see also Ueno et al., 2004). The presence of coarsely crystalline barite in veins together with black silica and sphalerite supports a hydrothermal origin for the barite, as does the acid–sulfate alteration of footwall basalts that indicates intense, high-sulfidation hydrothermal alteration under shallow water, to subaerial, low-temperature conditions (Kojima et al., 1998; Van Kranendonk and Pirajno, 2004; Van Kranendonk, 2006).

Whereas Lambert et al. (1978) argued in favour of surface oxidation of reduced magmatic fluids to account for the large volumes of sulfate in the Dresser Formation, and inferred bacterial oxidation "...by blue-green algae or sulfur bacteria." (p. 810), the presence of large volumes of barite as a primary mineral in sub-seafloor veins, the very large volume and coarse crystallinity of barite, and its direct association with ongoing hydrothermal processes within the formation indicates that sulfate concentration was likely a byproduct of acid–sulfate alteration (Van Kranendonk, 2006). In this scenario, dissolved gasses in the magmatic vapour plume (H_2S) reacted with cool, shallow meteoric water and seawater (H_2O) to produce H_2SO_4 through sulfur disproportionation (cf. Gamo et al., 1997), according to the reaction:

$$H_2S + 4H_2O = H_2SO_4 + 8H^+$$

At shallow levels and low hydrothermal temperatures (100–200 °C: Ueno et al., 2004), these reactions cause steam-heated acid–sulfate (advanced argillic) alteration that liberated almost all components of the host rocks into the hydrothermal fluids, including Ba from feldspars in basalt that combined with the acid to precipitate barite. It is important to note that in this scenario, there is no requirement for oxidation by biological mediation to account for the barite, supporting the results from previous sulfur isotope studies on barite, which show magmatic compositions of +3.6‰ (Lambert et al., 1978). Indeed, the widespread development of advanced argillic alteration, as represented by the development of hydrothermal kaolinite around the Dresser Mine (Van Kranendonk and Pirajno, 2004), suggests that barite crystallization occurred during periods of hydrothermal circulation under very shallow water to subaerial conditions (Fig. 24: Buchanan, 1981). However, the presence of mass-independent isotopic signatures of sulfur in samples from the Dresser Formation indicates that at least some of the sulfate in the system may have originate through photochemical oxidation of volcanogenic sulfur species in the atmosphere (cf. Farquhar et al., 2000; Philippot et al., 2007).

Two other observations support a very shallow water, low temperature, hydrothermal system. One is the local presence of bladed calcite in the drillcore (Fig. 9f), which is characteristic of epithermal systems (Pirajno, 1992). The other is the discovery of hydrothermal aragonite with colloform banding in the former gypsum(?) crystal rosettes in bedded carbonate rocks of regional section C (Fig. 23c and d). The colloform texture indicates that the aragonite was precipitated as a hydrothermal replacement of the original gypsum(?) and is important because it represents the lowest temperature part

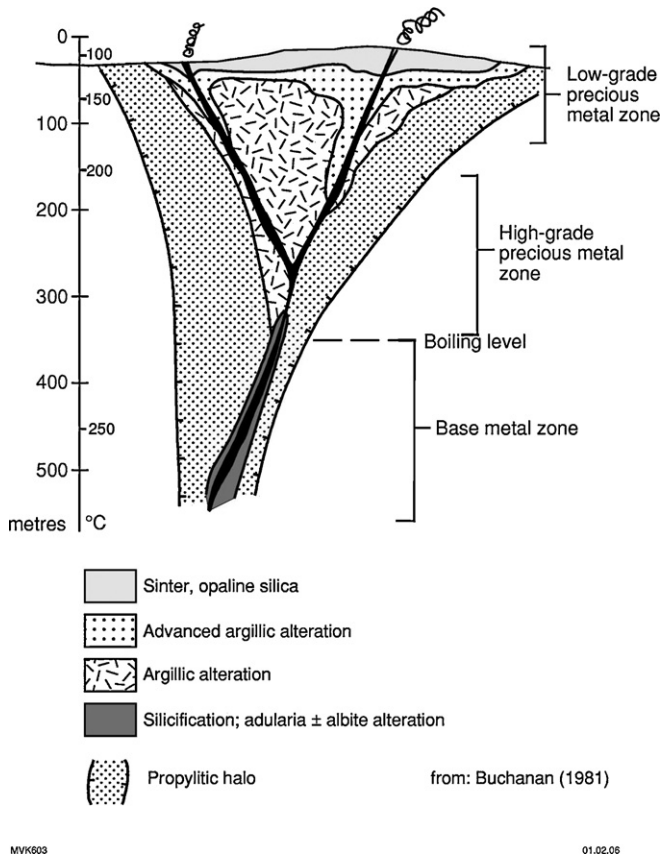

Fig. 24. Schematic cross-section of a hot spring depositional model, according to Buchanan (1981). The zone of advanced argillic alteration is characterised by alunite, kaolin and pyrite.

of the hydrothermal system, with precipitation under temperatures of ~50–80 °C (Deer et al., 1966).

The drillcore samples show that silica + barite + pyrite hydrothermal alteration ceased after deposition of member 4. A distinct style of hydrothermal alteration was responsible for precipitation of carbonate–chlorite–rutile assemblages in member 6 and for the formation of dissolution breccias in that member. A similar alteration mineral assemblage in immediately overlying basalts suggests that these hydrothermal fluids derived from heat of eruption of the overlying basalts, in a similar manner as has been suggested for the alteration of the Strelley Pool Chert higher up in the stratigraphy (Van Kranendonk and Pirajno, 2004).

Haematite alteration of carbonate rocks at the top of member 6 appears to be related to flushing of Fe-rich carbonate rocks by silica-rich fluids. Whereas silica flushing may represent a different part of the chlorite–carbonate–rutile alteration style, it may also represent the results of a different process, as these rocks do not appear to contain the carbonate–chlorite–rutile assemblage.

6.3. Redox state of the early Archean atmosphere/hydrosphere

Two observations combine to suggest that deposition of the Dresser Formation occurred under reducing conditions. First is the presence of Fe-rich carbonates throughout the formation, which suggests primary marine carbonate deposition under strongly reducing conditions (cf. Ohmoto et al., 2004). We consider the highly reducing and CO_2-saturated early Archean oceans to have been slightly acidic and thus able to etch and replace quartz sand grains found within member 1 of the Dresser Formation by carbonate within the oceanic (not metamorphic) realm.

Second is the presence of pyrite throughout the section. It occurs as small diagenetic crystals in carbonate sedimentary rocks, as a widespread replacement mineral of bedded carbonate, as possible primary precipitates in members 1 and 2, and as alteration rims on detrital sand grains in members 1 and 3 (e.g., Fig. 9b). This indicates sediment accumulation under reducing conditions, with high concentrations of H_2S and Fe (and CO_2 and CH_4) in the system, as has also been identified from fluid inclusion (Lambert et al., 1978; Foriel et al., 2004) and carbon isotopic studies (Ueno et al., 2006).

Periods of high H_2S and Fe input from hydrothermal fluids during pyrite precipitation alternated with periods of barite crystallization during the accumulation and alteration of members 1–4. This indicates alternating hydrothermal fluid conditions, as independently recognised from the fluid inclusion studies of Foriel et al. (2004). However, the presence of barite does *not* indicate oxidizing conditions, as sulfates can arise from the interaction of reducing sulfide-bearing fluids with cool seawater (as discussed above and in Van Kranendonk, 2006) and through photochemical oxidation of volcanogenic sulfur species (Farquhar et al., 2000).

The presence of haematite as both detrital grains in sandstone in member 1 and as bedded jasper interlayered with carbonates at the top of member 6 poses an apparent problem with a reducing condition of deposition inferred above from the ubiquitous presence of pyrite. Ohmoto (2003), for example, has used the presence of haematite in the stratigraphically overlying Marble Bar Chert Member of the Duffer Formation to argue in support of oxidizing Archean conditions.

However, textural evidence from member 6 suggests that the haematite originated as an alteration product of sedimentary Fe-carbonate, when these rocks were flushed by silica-saturated hydrothermal fluids, and did not form as primary haematite precipitates directly from seawater. Haematite alteration is restricted to the topmost part of the section, at the contact with overlying basalt, even though Fe-rich carbonate is present lower down in the section. This evidence is used to suggest that the generation of haematite was the result of hydrothermal fluid alteration from fluids heated up, and driven down into the footwall during eruption of the overlying basalt.

Regardless which of these models regarding the origin of the haematite is correct, the fact that diagenetic pyrite crystals have remained stable during haematite alteration (e.g., Fig. 17b) suggests that the formation of haematite was *not* due to oxidation, as suggested by Ohmoto (2003). Rather, we suggest that the hydrothermal fluids (and general atmospheric conditions) were reducing and that haematite alteration of Fe-carbonate was the result of circulating hydrothermal fluids that increased the pH of the system and liberated Fe from the siderite lattice during recrystallization (upper horizontal arrow in Fig. 25: cf. Garrels and Christ, 1965). This concept explains how pyrite remained stable during this alteration event (lower horizontal arrow in Fig. 25). An alternative origin of the jasper through microbial precipitation cannot be ruled out at this stage.

6.4. Depositional model

As outlined in Section 1, there are three competing models for the depositional environment of the Dresser Formation.

Recent studies by Nijman et al. (1998) and Van Kranendonk (2006) have shown that deposition of the Dresser Formation was in a much more tectonically active setting than the quiet lagoon model suggested by Groves et al. (1981) and Buick and Dunlop (1990). Several previous observations also clearly counter the model of thrust-bound ophiolite slices.

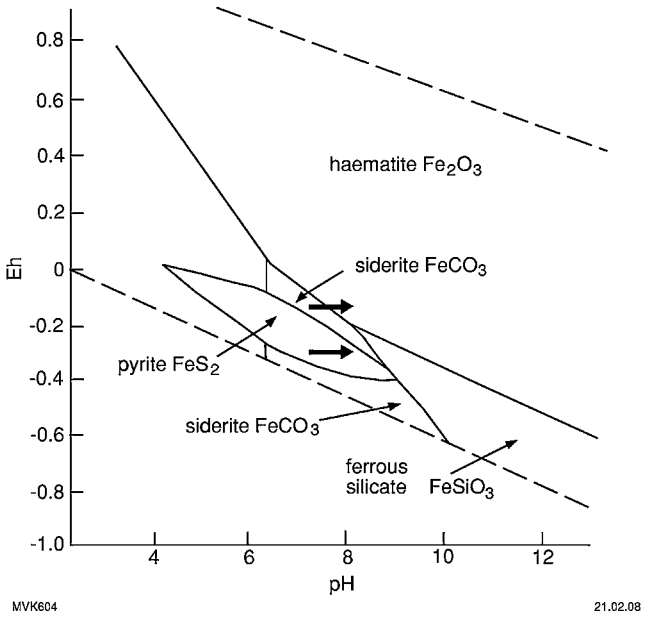

Fig. 25. Stability fields for iron minerals. Eh vs. pH relationships at 25 °C and 1 atm (redrawn from Garrels and Christ, 1965). Heavy arrows denote proposed fluid pathway to account for the transition from siderite to haematite.

(1) The acid–sulfate style of hydrothermal alteration, the evidence for shallow water to subaerial conditions, and the presence of felsic volcanic material in the Dresser Formation all combine to preclude a mid-ocean ridge setting.
(2) If thrusting did occur at some point after deposition of the Dresser Formation, as proposed in this model, then deformation would have been concentrated in the rheologically weakest part, namely the hydrothermally altered footwall. However, this is not the case as contacts between the lower chert–barite unit of the Dresser Formation and overlying pillow basalts are demonstrably autochthonous in sections A–F, as well as in the drillcore sections described in this study (see also Van Kranendonk, 2006). Furthermore, the top contact of the chert–barite unit is also demonstrably autochthonous, as there is no evidence of fault displacement evident either in outcrop (e.g., regional section C) or in drillcore sections.
(3) Ages of greenstones return progressively younger U–Pb zircon age dates up section, from ca. 3490–3480 Ma in the Dresser Formation (Thorpe et al., 1992b; this paper), to 3470 ± 2 Ma in the Antarctic Creek Member of the Mount Ada Basalt (Byerly et al., 2002), to ca. 3459–3434 Ma in the Panorama Formation (Thorpe et al., 1992a; Nelson, 2000) (see Fig. 2). These data preclude older-over-younger stacking of greenstones.
(4) The observation of repeated downward-increasing metamorphic temperature profiles in North Pole greenstones can be explained by the model of repeated hydrothermal fluid circulation presented in Van Kranendonk (2006).
(5) The dextral fault set that affect the Dresser Formation in the northwestern part of the dome (cf. Ueno et al., 2001a,b) is not uniquely indicative of thrusting. A more likely model is that these faults formed as a result of dextral strike-slip deformation during regional transpressional deformation at ca. 2930 Ma (Van Kranendonk et al., 2002, 2004).

Instead, the presence of internal unconformities within the drillcore section, combined with evidence for active growth faulting and for repeated episodes of felsic volcanism and hydrothermal fluid circulation during sediment accumulation, strongly support deposition of the lower chert–barite unit of the Dresser Formation in the caldera of an active felsic volcano (Nijman et al., 1998; Nijman and de Vries, 2004; Van Kranendonk and Pirajno, 2004; Van Kranendonk, 2006).

Results from previous work and from the results presented herein provide the basis for a more detailed depositional model (Fig. 26). Surface and drillcore sections through the Dresser Formation chert–barite unit support its division into six members that represent three principal episodes of sedimentation (Figs. 3 and 21). A lower sedimentary unit of finely bedded carbonates and minor sandstone (member 1) was deposited unconformably on footwall basalts. Episodes of intermediate to felsic volcanism and of pyrite–barite–silica hydrothermal alteration accompanied this member, as indicated by the coarse breccia in section D, which has barite blocks in a felsic volcaniclastic matrix, and by the presence of barite and intermediate to felsic volcanic clasts in sandstone in PDP2b (Fig. 23a). Active growth faulting commenced at this time, producing a deeper water basin in the central and northern parts of the basin, separated by a highstand.

Deposition continued to shallow water conditions, as indicated by the presence of rippled carbonate sandstones near the top of member 1, and then to very shallow water and even local subaerial conditions when stromatolites flourished, as represented by member 2. The fact that the thickest section of wrinkly stromatolitic laminates occurs in an area of thin overall stratigraphy may indicate proximity to the shallow margin of the basin at this locality. Evidence of the diagenetic growth of gypsum(?) crystal rosettes in rocks immediately beneath the interval with evidence of deposition under shallow water to subaerial conditions suggests a period of high evaporation (cf. Groves et al., 1981; Buick and Dunlop, 1990) of seawater with an end member salinity three to four times that of modern seawater (Foriel et al., 2004). The relative thinness of the stratigraphic succession, combined with the evidence for block faulting, suggests that shallowing at this time was the result of surface uplift rather than basin filling (Stage 1 in Fig. 26). Surface uplift was probably the result of emplacement of shallow subvolcanic magmas preceding the main period of volcanic eruption, as documented for other lacco-calderas (cf. Henry et al., 1997; Breitkreuz and Petford, 2004).

Trace element analysis of carbonates indicates precipitation of ankerite under anoxic conditions from marine water that had a strong hydrothermal component (Van Kranendonk et al., 2003) and was rich in dissolved salts (Foriel et al., 2004). The shallow to very shallow water depth during the main period of stromatolite growth (member 2), together with the coniform to columnar shape of many stromatolites at this level, suggests phototrophy.

The second depositional episode represents the main eruptive and hydrothermal circulation events in the caldera (Stages 2 and 3 in Fig. 26). The lower part of this episode is marked by deposition of a coarse felsic volcanic conglomerate (member 3), extensive growth faulting and soft-sediment deformation, and the widespread precipitation of hydrothermal pyrite–barite–chert–sphalerite. Good evidence of the synchronous nature of growth faulting and deposition of coarse conglomerate units is provided by the centimetre-wide hot slump fault that separates the two subunits of member 3. Given the proximal nature of felsic volcanism in this member – as represented by welded tuffs and the coarse, unsorted nature of the breccias – and the hot, ductile nature of the chlorite–pyrite–rutile shear zone in what is otherwise a very low-grade series of rocks, this zone is interpreted to represent a slump fault, or tectonic slide, associated with a volcanic eruptive event.

Hydrothermal fluid circulation at this time was part of a high-sulfidation system that caused extensive alteration of the footwall (Stage 3 in Fig. 26). The alteration is zoned from higher temperatures lower down in the system (propylitic alter-

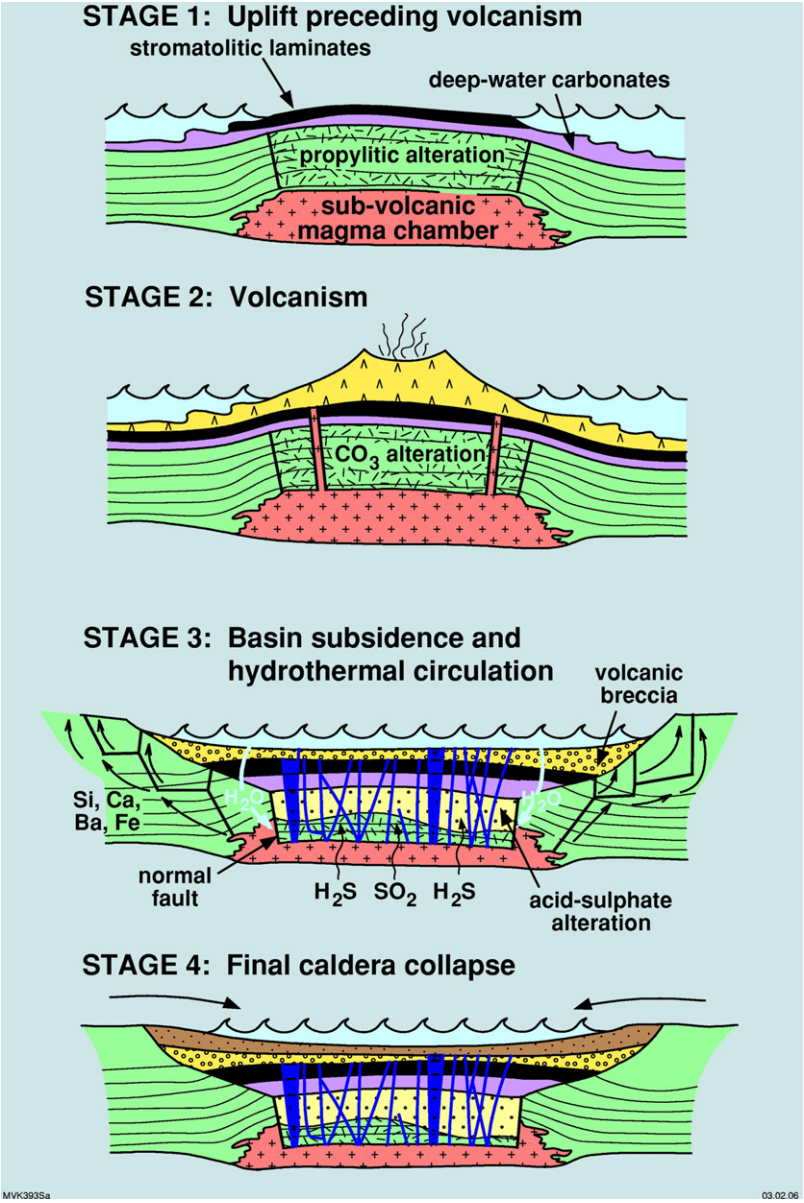

Fig. 26. Schematic model of deposition of the Dresser Formation through four principal stages: (1) deposition of carbonates from deep water through to shallow water conditions during surface uplift due to inflation of the subvolcanic felsic magma chamber; (2) the main eruptive period of felsic volcanic material; (3) post-eruptive hydrothermal circulation and heterogeneous basin subsidence across normal growth faults; (4) final caldera collapse and infilling of the basin by clastic detritus. Felsic volcanism accompanies each of the stages shown.

ation, ~250–350 °C), through a zone of steam-heated acid–sulfate alteration (advanced argillic alteration, ~100–200 °C: cf. Van Kranendonk and Pirajno, 2004), to lower temperatures at the surface (hydrothermal aragonite, ~50–80 °C). Precipitation of hydrothermal minerals occurred primarily in the subsurface through replacement of bedded carbonate rocks and crack-seal emplacement of veins, as documented for other, more recent barite–sulfide deposits (cf. Kelley et al., 2004). The hydrothermal system was dynamic and complex, with probable mixing of fluids from different sources, including magmatic fluids, seawater, and meteoric water during periods of very shallow water to subaerial conditions (see Fig. 29 in Van Kranendonk, 2006). Mixing of rising hydrothermal fluids with low-temperature meteoric fluids and seawater was probably facilitated by drawdown of the latter along growth faults, following the model of Stix et al. (2003).

Deposition of coarse conglomerates gave way to quiet water precipitation of carbonates in deeper water parts of the caldera (member 4), followed by renewed episodes of hydrothermal fluid circulation that precipitated barite and chert in massive veins. At some time during this second episode, the rocks were once again exposed to subaerial conditions (at least locally), as indicated by the unconformity at the base of member 5 that is evident in the drillcores from PDP2 described above.

The absence of member 4 in both drillholes, and of member 3 in drillhole PDP2b contrasts with the presence of all six members in surface outcrops 100 m away. This excision of stratigraphy across short distances indicates significant tectonic disturbance and tilting of members 1–4 prior to deposition of member 5. Based on these observations, the direction of tilting at the drillsite locality was to the north, towards the centre of the caldera, consistent with the idea that tilting was due to caldera collapse.

The presence of tourmaline crystals and white mica flakes immediately above the basal unconformity of member 5 in PDP2c supports a period of subaerial exposure at this time and concentration of Boron from seawater derived through weathering of exposed felsic igneous rocks. Subaerial exposure is confirmed by previous observations of desiccation cracks in mudstones along strike (Lambert et al., 1978; Van Kranendonk, 2006), and by the low-temperature estimates for the steam-heated acid–sulfate alteration system (e.g., Fig. 24).

The fact that barite-rich hydrothermal fluids did not affect member 5, combined with the unconformity at the base of this member, suggests a significant break in depositional history and change in the nature of hydrothermal processes across this boundary. However, the evidence of felsic volcanism in member 5, and siliceous hydrothermal alteration of member 6 provides indirect links between these upper members and the underlying members of the formation.

The final episode of sediment deposition occurred under renewed basin subsidence, as indicated by fining upwards succession from sandstone to quiet water carbonates (members 5 and 6) (Stage 4 in Fig. 26). Member 5 is correlated with the upper transgressive sand sheet of Nijman et al. (1998), which they inferred was related to deposition during a return to deeper water conditions as a prelude to the renewal of basaltic volcanism. Continued subsidence to quiet water conditions (member 6) was accompanied by the final phase of felsic volcanism, as indicated by the felsic volcaniclastic sandstone in PDP2c.

Carbonate deposition during accumulation of member 6 was dominantly under quiet water conditions, as indicated by the presence of very fine bedding of micritic carbonates and by the general lack of terrigenous material. However, the presence of quartz flakes and detrital sand grains at 93.1 m depth in PDP2c suggests a period of input from a felsic source. Certainly, periods of continued – though relatively mild – tectonic instability during sediment accumulation are indicated by the presence of local unconformities in otherwise fine bedding (e.g., Fig. 13b). The thickest part of this member occurs in the area of the Dresser Mine (section E), in the heart of the underlying hydrothermal system. This evidence is used to infer that basin subsidence was the result of the end of eruption and final sinking of the caldera (Stage 4 in Fig. 26).

These rocks were not affected by the hydrothermal alteration associated with the lower units. Rather, the coarse crystalline carbonate–chlorite–rutile veins and breccias in the upper part of member 6 are interpreted to be the product of circulation of hydrothermal fluid with a distinct composition from those which affected the underlying rocks. The carbonate–chlorite–rutile mineral assemblage of this fluid phase is identical to the alteration mineral assemblage in the overlying basalts, suggesting that the fluids were derived from, and/or had passed through, the overlying basalts. The carbonate breccias in member 6 are similar to dissolution cavities formed in Phanerozoic carbonates as a result of circulating groundwater (cf. Groves et al., 1981; see Eliassen and Talbot, 2005). Haematite alteration appears to be associated with these fluids, as it is most intensely developed at the top of member 6, although other possible origins for the presence of haematite are still under investigation.

6.5. Environment(s) of putative life

Stromatolitic forms have been observed at three stratigraphic levels in the Dresser Formation. In member 1, mat-like, domical, columnar and coniform stromatolites have been described from outcrop exposures of silicified carbonates (Walter et al., 1980; Buick et al., 1981; Van Kranendonk, 2006) and in drillcore (e.g., Figs. 7a and 8a). Thin section observations of drillcore material show that these stromatolites are composed primarily of pyrite, but also that the pyrite was a replacement mineral of carbonate (e.g., Fig. 8b). Widespread wrinkly stratiform stromatolites and small to large domical stromatolites preserved in member 2 have also been extensively replaced by pyrite. Wrinkly stratiform stromatolites have also been observed in surface exposures of member 4.

Isotopic data shows that the pyrite in laminated sulfides is demonstrably hydrothermal in origin (Lambert et al., 1978) and thus unrelated to the carbonate in which the stromatolites formed, which has a marine signature (Van Kranendonk et al., 2003). Significantly, most stromatolite-like forms cannot be related to the growth of diagenetic or hydrothermal minerals.

Of interest is the fact that carbonates with stromatolitic forms are much more heavily replaced by pyrite than carbonates with simple planar bedding. This preferential replacement of stromatolitic carbonates by pyrite may result either from iron extraction from circulating hydrothermal solutions by reduced organic material, or an exceptional degree of pyrite formation through microbial means.

A second line of evidence in support of early life in these rocks occurs in member 6, in the form of micritic carbonate beds that contain clasts of laminated to clotty-textured carbonaceous matter (e.g., Fig. 14d).

Diagenetic dolomite rhombs and euhedral pyrite crystals in micritic carbonate of member 6 (Fig. 14c and e) may be further signs of early life, as both are known to result from microbial activity in modern sediments (e.g., Berner, 1970; Vasconcelos and McKenzie, 1997).

Shen et al. (2001) argued for the presence of sulfate-reducing bacteria in rocks from the Dresser Formation, on the basis of depleted $\delta^{34}S$ values of pyrite from growth zones in barite (e.g., Fig. 7d). However, Philippot et al. (2007) discounted this possibility and suggested on the basis of detailed sulfur isotope studies from the drillcore material described in this paper that early Archean micro-organisms at North Pole preferred elemental sulfur, not sulfate.

7. Conclusions

Detailed stratigraphic and petrological data from an investigation of surface outcrops and diamond drillcore through the lowermost, ca. 3.5 Ga, chert–barite horizon of the Dresser Formation provide evidence of deposition within a volcanic caldera that was dominated by hydrothermal processes. Previous models of deposition within a quiet lagoon, or mid-ocean ridge setting, can be discounted. Deposition of Fe-carbonates commenced with periods of quiet water precipitation that were interspersed with periods of intense hydrothermal activity and felsic volcanism, accompanied by tectonic instability during episodes of growth faulting. Carbonate deposition continued to shallow water and intermittently exposed conditions, when stromatolites flourished. This was followed by the main period of caldera formation and hydrothermal fluid circulation, marked by coarse conglomerates, block faulting, soft-sediment deformation, and an erosional unconformity. Final caldera collapse resulted in deposition of sandstones and micritic carbonates.

Hydrothermal alteration of the footwall includes zones of propylitic, argillic and advanced argillic alteration, indicative of steam-heated acid–sulfate alteration under shallow water conditions. Alteration temperatures vary from 250 to 300 °C near the base of the system to 50–80 °C near the top, where hydrothermal aragonite was precipitated. Barite crystallized from multiple pulses of circulating hydrothermal fluids in veins in the altered footwall and as a replacement of carbonates in the sedimentary

succession. Sulfate precipitation due to evaporation – if it occurred at all – is restricted to a single horizon in member 1, beneath the stromatolites, where possible gypsum crystal rosettes are preserved.

Putative signs of life in the Dresser Formation include stromatolites of diverse morphology (mat-like, columnar, domical, and coniform), clasts of laminated carbonaceous material in bedded micritic carbonate (eroded microbial mats), and diagenetic crystals of pyrite and carbonate in bedded micritic carbonate. Stromatolites consist predominantly of pyrite of hydrothermal origin, but this was observed to be a replacement of carbonate. Stromatolitic structures cannot be correlated with crystal growth forms and thus provide a good morphological indicator of early life on Earth.

Acknowledgements

This project was supported by funds from the Institute de Physique du Globe de Paris (IPGP) and the CNRS, and by the Geological Survey of Western Australia (GSWA). Paul van Louwenhart of Mount Magnet drilling and his crew are thanked for their professional work and enthusiasm in obtaining the drillcore. In particular, we wish to thank John Ludden for his support of the project, and V. Courtillot (IPGP) and T. Griffin (GSWA) for supporting a visiting position for M. Van Kranendonk at the IPGP to work on thin sections of the drillcore. Zircon analyses were performed at the Western Australian SHRIMP-II facility, operated by a WA university-government consortium with the support of the Australian Research Council. Figures were drafted by S. Dowsett. Thanks to Ian Fletcher, Malcolm Walter, Adrian Brown and two anonymous reviewers for their comments that helped improve the manuscript. This paper is published with permission of the Executive Director of the GSWA. This is IPGP contribution No. 2416.

References

Allwood, A.C., Walter, M.R., Kamber, B.S., Marshall, C.P., Burch, I.W., 2006. Stromatolite reef from the Early Archaean era of Australia. Nature 441, 714–717.

Amelin, Y., Lee, D.-C., Halliday, A.N., 2000. Early-middle Archaean crustal evolution deduced from Lu–Hf and U–Pb isotopic studies of single zircon grains. Geochimica et Cosmochimica Acta 64, 4205–4225.

Awramik, S.M., Schopf, J.W., Walter, M.R., 1983. Filamentous fossil bacteria from the Archean of Western Australia. Precambrian Research 20, 357–374.

Awramik, S.M., Schopf, J.W., Walter, M.R., 1988. Carbonaceous filaments from North Pole, Western Australia: are they fossil bacteria in Archean stromatolites? A discussion. Precambrian Research 39, 303–309.

Berner, R.A., 1970. Sedimentary pyrite formation. American Journal of Science 208, 1–23.

Blewett, R.S., Shevchenko, S., Bell, B., 2004. The North Pole Dome: a non-diapiric dome in the Archaean Pilbara Craton, Western Australia. Precambrian Research 133, 105–120.

Brasier, M.D., Green, O.R., Jephcoat, A.P., Kleppe, A.K., Van Kranendonk, M.J., Lindsay, J.F., Steele, A., Grassineau, N., 2002. Questioning the evidence for Earth's oldest fossils. Nature 416, 76–81.

Brasier, M.D., Green, O.R., Lindsay, J.F., Steele, A., 2004. Earth's oldest (~3.5 Ga) fossils and the 'Early Eden hypothesis': questioning the evidence. Origins of Life and Evolution of the Biosphere 34, 257–269.

Breitkreuz, C., Petford, N. (Eds.), 2004. Physical Geology of High-level Magmatic Systems. Geological Society, Special Publication 234, 262 pp.

Brown, A.J., Cudahy, T.J., Walter, M.R., 2006. Hydrothermal alteration at the Panorama Formation, North Pole Dome, Pilbara Craton, Western Australia. Precambrian Research 151, 211–223.

Buchanan, L.J., 1981. Precious metal deposits associated with volcanic environments in the southwest. In: relations of tectonics to ore deposits: Arizona Geological Society, Digest XIV, 237–262.

Buick, R., 1984. Carbonaceous filaments from North Pole, Western Australia: are they fossil bacteria in Archean stromatolites? Precambrian Research 24, 157–172.

Buick, R., 1988. Carbonaceous filaments from North Pole, Western Australia: are they fossil bacteria in Archean stromatolites? A reply. Precambrian Research 39, 311–317.

Buick, R., 1990. Microfossil recognition in Archean rocks: an appraisal of spheroids and filaments from a 3500 M.Y. old chert–barite unit at North Pole, Western Australia. Palaios 5, 441–459.

Buick, R., Dunlop, J., 1990. Evaporitic sediments of early Archaean age from the Warrawoona Group, North Pole, Western Australia. Sedimentology 37, 247–277.

Buick, R., Dunlop, J.S.R., Groves, D.I., 1981. Stromatolite recognition in ancient rocks: an appraisal of irregular laminated structures in an early Archaean chert–barite unit from North Pole, Western Australia. Alcheringa 5, 161–181.

Buick, R., Thornett, J.R., McNaughton, N.J., Smith, J.B., Barley, M.E., Savage, M., 1995. Record of emergent continental crust ~3.5 billion years ago in the Pilbara Craton of Australia. Nature 375, 574–577.

Byerly, G.R., Lowe, D.R., Wooden, J.L., Xie, X., 2002. An Archean impact layer from the Pilbara and Kaapvaal Cratons. Science 297, 1325–1327.

Compston, W., Williams, I.S., Meyer, C., 1984. U–Pb geochronology of zircons from lunar breccia 73217 using a sensitive high mass-resolution ion microprobe. Journal of Geophysical Research 89, B252–B534.

Deer, W.A., Howie, R.A., Zussman, J., 1966. An Introduction to the Rock Forming Minerals. Longman Group Ltd., London, 528 pp.

Dunlop, J.S.R., Muir, M.D., Milne, V.A., Groves, D.I., 1978. A new microfossil assemblage from the Archaean of Western Australia. Nature 274, 676–678.

Eliassen, A., Talbot, M.R., 2005. Solution-collapse breccias of the Minkinfjellet and Wordiekammen Formations, Central Spitsbergen, Svalbard: a large gypsum palaeokarst system. Sedimentology 52, 775–794.

Farquhar, J., Bao, H., Thiemens, M., 2000. Atmospheric influence of Earth's earliest sulfur cycle. Science 289, 756–758.

Foriel, J., Philippot, P., Rey, P., Somogyi, A., Banks, D., Menez, B., 2004. Biological control of Cl/Br and low sulphate concentration in a 3.5 Gyr-old seawater from North Pole, Western Australia. Earth and Planetary Science Letters 228, 451–463.

Gamo, T., Okamura, K., Charlou, J.-L., et al., 1997. Acidic and sulfate-rich hydrothermal fluids from the Manus back-arc basin, Papua New Guinea. Geology 25, 139–142.

Garcia-Ruiz, J.M., Hyde, S.T., Carnerup, A.M., Christy, A.G., Van Kranendonk, M.J., Welham, N.J., 2003. Self-assembled silica–carbonate structures and detection of ancient microfossils. Science 302, 1194–1197.

Garrels, R.M., Christ, C.L., 1965. Solutions, Minerals and Equilibria. Harper Press, 450 pp.

Grotzinger, J.P., Rothman, D.R., 1996. An abiotic model for stromatolite morphogenesis. Nature 383, 423–425.

Groves, D.I., Dunlop, J.S.R., Buick, R., 1981. An early habitat of life. Scientific American 245, 64–73.

Henry, C.D., Kunk, M.J., Muehlberger, W.R., McIntosh, W.C., 1997. Igneous evolution of a complex laccolith–caldera, the Solitario, Trans-Pecos, Texas: implications for calderas and subjacent plutons. Geological Society of America Bulletin 109, 1036–1054.

Hickman, A.H., 1973. The North Pole barite deposits, Pilbara Goldfield: Western Australia Geological Survey, Annual Report 1972, pp. 57–60.

Hickman, A.H., 1983. Geology of the Pilbara Block and its environs: Western Australia Geological Survey, Bulletin 127, 268 pp.

Hodgson, C.J., 1989. The structure of shear-related, vein-type gold deposits: a review. Ore Geology Reviews 4, 231–273.

Hofmann, H.J., Grey, K., Hickman, A.H., Thorpe, R., 1999. Origin of 3.45 Ga coniform stromatolites in the Warrawoona Group, Western Australia. Geological Society of America Bulletin 111, 1256–1262.

Kelley, K.D., Dumoulin, J.A., Jennings, S., 2004. The Anarraaq Zn–Pb–Ag and barite deposit, northern Alaska: evidence for replacement of carbonate by barite and sulphides. Economic Geology 99, 1577–1591.

Kitajima, K., Maruyama, S., Utsonomita, S., Liou, J.G., 2001a. Seafloor hydrothermal alteration at an Archaean mid-ocean ridge. Journal of Metamorphic Geology 19, 581–597.

Kitajima, K., Kabashima, T., Ueno, Y., Terabayashi, M., Maruyama, S., 2001b. Archaean seafloor hydrothermal system in the North Pole of the Pilbara Craton, Western Australia. In: Cassidy, K.F., Dunphy, J.M., Van Kranendonk, M.J. (Eds.), Proceedings of the Fourth International Archaean Symposium, Extended Abstracts, AGSO – Geoscience Australia Record 2001/37, pp. 51–53.

Knauth, L.P., Lowe, D.R., 2003. High Archaean climatic temperature inferred from oxygen isotope geochemistry of cherts in the 3.5 Ga Swaziland Supergroup, South Africa. Geological Society of America Bulletin 115, 566–580.

Kojima, S., Hanamuro, T., Hayashi, K., Haruna, M., Ohmoto, H., 1998. Sulphide minerals in Early Archaean chemical sedimentary rocks of the eastern Pilbara district, Western Australia. Mineralogy and Petrology 64, 219–235.

Lambert, I., Donnelly, T., Dunlop, J., Groves, D., 1978. Stable isotopic compositions of early Archaean sulphate deposits of probable evaporitic and volcanogenic origins. Nature 276, 808–811.

Lindsay, J.F., Brasier, M.D., McLoughlin, N., Green, O.R., Fogel, M., Steele, A., Mertzman, S.A., 2005. The problem of deep carbon—an Archaean paradox. Precambrian Research 143, 1–22.

Lowe, D.R., 1994. Abiological origin of described stromatolites older than 3.2 Ga. Geology 22, 387–390.

Ludwig, K.R., 2001. SQUID 1.02: A User's Manual. Berkeley Geochronology Center Special Publication 2.

Ludwig, K.R., 2003. Isoplot 3.00: A Geochronological Toolkit for Microsoft Excel. Berkeley Geochronology Center Special Publication 4.

McCollom, T.M., 2003. Formation of meteorite hydrocarbons from thermal decomposition of siderite ($FeCO_3$). Geochimica et Cosmochimica Acta 67, 311–317.

Nelson, D.R., 1998. Compilation of SHRIMP U–Pb zircon geochronology data, 1997. Geological Survey of Western Australia, Record 1998/2, 242 pp.

Nelson, D.R., 2000, Compilation of geochronology data, 1999: Geological Survey of Western Australia, Record 2000/2, 251 pp.

Nijman, W., De Bruin, K., Valkering, M., 1998. Growth fault control of early Archaean cherts, barite mounds, and chert–barite veins, North Pole Dome, Eastern Pilbara, Western Australia. Precambrian Research 88, 25–52.

Nijman, W., de Vries, S.T., 2004. Early Archaean crustal collapse structures and sedimentary basin dynamics. In: Eriksson, P.G., Altermann, W., Nelson, D.R., Mueller, W.U., Catuneanu, O. (Eds.), The Precambrian Earth: Tempos and Events. Elsevier, pp. 139–154.

Ohmoto, H., 2003. Chemical and biological evolution of the early Earth: a minority report. Abstracts of the 13th Annual V.M. Goldschmidt Conference, Kurashiki, Japan. Geochimica et Cosmochimica Acta, A2, special supplement.

Ohmoto, H., Watanabe, Y., Kumazawa, K., 2004. Evidence from massive siderite beds for a CO_2-rich atmosphere before ~1.8 billion years ago. Nature 429, 395–399.

Philippot, P., Van Zuilen, M., Lepot, K., Thomazo, C., Farquhar, J., Van Kranendonk, M., 2007. Early Archean microorganisms preferred elemental sulphur, not sulphate. Science 317, 1534–1537.

Pirajno, F., 1992. Hydrothermal Mineral Deposits. Springer-Verlag, 709p.

Pirajno, F., Van Kranendonk, M.J., 2005. A review of hydrothermal processes and systems on earth and implications for Martian analogues. Australian Journal of Earth Sciences 52, 329–351.

Runnegar, B., Dollase, W.A., Ketcham, R.A., Colbert, M., Carlson, W.D., 2001. Early Archaean sulfates from Western Australia first formed as hydrothermal barites not gypsum evaporates. In: Annual Meeting and Exposition, Abstracts. Geological Society of America, p. A404.

Rye, R.O., 1993. The evolution of magmatic fluids in the epithermal environment: the stable isotope perspective. Economic Geology 88, 733–753.

Schopf, J.W., 1993. Microfossils of the Early Archaean Apex Chert: new evidence of the antiquity of life. Science 260, 640–646.

Schopf, J.W., Kudryavtsev, A.B., Agresti, D.G., Wdowiak, T.J., Czaja, A.D., 2002. Laser-Raman imagery of Earth's earliest fossils. Nature 416, 73–76.

Schopf, J.W., Kudryavtsev, A.B., Czaja, A.D., Tripathi, A.B., 2007. Evidence of Archean life: stromatolites and microfossils. Precambrian Research 158, 141–155.

Shen, Y., Buick, R., Canfield, D.E., 2001. Isotopic evidence for microbial sulphate reduction in the early Archaean era. Nature 410, 77–81.

Smithies, R.H., Van Kranendonk, M.J., Champion, D.C., 2005. It started with a plume—Early Archaean basaltic proto-continental crust. Earth and Planetary Science Letters 238, 284–297.

Smithies, R.H., Champion, D.C., Van Kranendonk, M.J., Hickman, A.H., 2007. Geochemistry of volcanic rocks of the northern Pilbara Craton. Western Australia Geological Survey, Report 104, 47 pp.

Stacey, J.S., Kramers, J.D., 1975. Approximation of terrestrial lead isotope evolution by a two-stage model. Earth and Planetary Science Letters 26, 207–221.

Steiger, R.H., Jäger, E., 1977. Subcommission on geochronology: convention on the use of decay constants in geo- and cosmochronology. Earth and Planetary Science Letters 36, 359–362.

Stix, J., Kennedy, B., Hannington, M., Gibson, H., Fiske, R., Mueller, W., Franklin, J., 2003. Caldera-forming processes and the origin of submarine volcanogenic massive sulphide deposits. Geology 31, 375–378.

Terabayashi, M., Masuda, Y., Ozawa, H., 2003. Archaean ocean floor metamorphism in the North Pole area, Pilbara Craton, Western Australia. Precambrian Research 127, 167–180.

Thiry, M., Milnes, A.R., Véronique, R., Simon-Coinçon, R., 2006. Interpretation of paleoweathering features and successive silicification in the Tertiary regolith of inland Australia. Journal of the Geological Society of London 163, 723–736.

Thorpe, R.A., Hickman, A.H., Davis, D.W., Mortensen, J.K., Trendall, A.F., 1992a. U–Pb zircon geochronology of Archaean felsic units in the Marble Bar region, Pilbara Craton, Western Australia. Precambrian Research 56, 169–189.

Thorpe, R.I., Hickman, A.H., Davis, D.W., Mortensen, J.K., Trendall, A.F., 1992b. Constraints to models for Archaean lead evolution from precise U–Pb geochronology from the Marble Bar region, Pilbara Craton, Western Australia. In: Glover, J.E., Ho, S. (Eds.), The Archaean: Terrains, Processes and Metallogeny. Geology Department and University Extension, The University of Western Australia, Publication 22, pp. 395–408.

Ueno, Y., Isozaki, Y., Yurimoto, H., Maruyama, S., 2001a. Carbon isotopic signatures of individual Archaean microfossils(?) from Western Australia. International Geology Reviews 43, 196–212.

Ueno, Y., Maruyama, S., Isozaki, Y., Yurimoto, H., 2001b. Early Archaean (ca. 3.5 Ga) microfossils and ^{13}C-depleted carbonaceous matter in the North Pole area, Western Australia: field occurrence and geochemistry. In: Nakashima, S., Maruyama, S., Brack, A., Windley, B.F. (Eds.), Geochemistry and the Origin of Life. Universal Academic Press, pp. 203–236.

Ueno, Y., Yoshioka, H., Maruyama, S., Isozaki, Y., 2004. Carbon isotopes and petrography in ~3.5 Ga hydrothermal silica dykes in the North Pole area, Western Australia. Geochimica et Cosmochimica Acta 68, 573–589.

Ueno, Y., Yamada, K., Yoshida, N., Maruyama, S., Isozaki, Y., 2006. Evidence from fluid inclusions for microbial methaogenesis in the early Archaean era. Nature 440, 516–519.

van de Graaff, W.J.E., 1983. Silcrete in Western Australia: geomorphological settings, textures, structures, and their genetic implications. In: Wilson, R.C.L. (Ed.), Residual Deposits: Surface Related Weathering Processes and Materials. Geological Society of London, Special Publication 11, pp. 159–166.

Van Kranendonk, M.J., 2000. Geology of the North Shaw 1:100 000 sheet. Western Australia Geological Survey, 1:100 000 series explanatory notes.

Van Kranendonk, M.J., 2006. Volcanic degassing, hydrothermal circulation and the flourishing of early life on Earth: new evidence from the Warrawoona Group, Pilbara Craton, Western Australia. Earth Science Reviews 74, 197–240.

Van Kranendonk, M.J., 2007. A review of the evidence for putative Paleoarchean life in the Pilbara Craton. In: Van Kranendonk, M.J., Smithies, R.H., Bennet, V. (Eds.), Earth's Oldest Rocks. Developments in Precambrian Geology, vol. 15. Elsevier, Amsterdam, pp. 855–896.

Van Kranendonk, M.J., Pirajno, F., 2004. Geological setting and geochemistry of metabasalts and alteration zones associated with hydrothermal chert ± barite deposits in the ca. 3.45 Ga Warrawoona Group, Pilbara Craton, Australia. Geochemistry: Exploration, Environment, Analysis 4, 253–278.

Van Kranendonk, M.J., Hickman, A.H., Williams, I.R., Nijman, W., 2001. Archaean geology of the East Pilbara Granite-Greenstone Terrane, Western Australia—a field guide. Western Australia Geological Survey, Record 2001/9, 134 pp.

Van Kranendonk, M.J., Hickman, A.H., Smithies, R.H., Nelson, D.N., Pike, G., 2002. Geology and tectonic evolution of the Archaean North Pilbara terrain, Pilbara Craton, Western Australia. Economic Geology 97, 695–732.

Van Kranendonk, M.J., Webb, G.E., Kamber, B.S., 2003. Geological and trace element evidence for a marine sedimentary environment of deposition and biogenicity of 3.45 Ga stromatolitic carbonates in the Pilbara Craton, and support for a reducing Archean ocean. Geobiology 1 (2), 91–108.

Van Kranendonk, M.J., Hickman, A.H., Smithies, R.H., Williams, I.R., Bagas, L., Farrell, T.R., 2006a. Revised lithostratigraphy of Archaean supracrustal and intrusive rocks in the northern Pilbara Craton, Western Australia: Western Australia Geological Survey, Record 2006/15, 57 pp.

Van Kranendonk, M.J., Philippot, P., Lepot, K., 2006b. The Pilbara Drilling Project: c. 2.72 Ga Tumbiana Formation and. 3.49 Ga Dresser Formation, Pilbara Craton, Western Australia. Western Australia Geological Survey, Record 2006/14, 25 pp.

Van Kranendonk, M.J., Smithies, R.H., Hickman, A.H., Champion, D.C., 2007. Secular tectonic evolution of Archaean continental crust: interplay between horizontal and vertical processes in the formation of the Pilbara Craton, Australia. Terra Nova 19 (1), 1–38.

Vasconcelos, C., McKenzie, J.A., 1997. Microbial mediation of modern dolomite precipitation and diagenesis under anoxic conditions (Lagoa Vermelha, Rio de Janeiro, Brazil). Journal of Sedimentary Research 67, 378–390.

Walter, M.R., 1983. Archean stromatolites: evidence of the Earth's oldest benthos. In: Schopf, J.W. (Ed.), Earth's Earliest Biosphere. Princeton University Press, pp. 187–213.

Walter, M.R., Buick, R., Dunlop, J.S.R., 1980. Stromatolites, 3,400–3,500 Myr old from the North Pole area, Western Australia. Nature 284, 443–445.